IMPACT OF ROTOR SURFACE VELOCITY, LEAKAGE MODELS AND REAL GAS PROPERTIES ON ROTORDYNAMIC FORCE PREDICTIONS OF GAS LABYRINTH SEALS

A Thesis

by

MANISH RAMBHAU THORAT

Submitted to the Office of Graduate Studies of
Texas A&M University
in partial fulfillment of the requirements for the degree of

MASTER OF SCIENCE

May 2010

Major Subject: Mechanical Engineering

IMPACT OF ROTOR SURFACE VELOCITY, LEAKAGE MODELS AND REAL GAS PROPERTIES ON ROTORDYNAMIC FORCE PREDICTIONS OF GAS LABYRINTH SEALS

A Thesis

by

MANISH RAMBHAU THORAT

Submitted to the Office of Graduate Studies of
Texas A&M University
in partial fulfillment of the requirements for the degree of

MASTER OF SCIENCE

Approved by:

Chair of Committee,	Dara Childs
Committee Members,	Gerald Morrison
	Paul Cizmas
Head of Department,	Dennis L. O'Neal

May 2010

Major Subject: Mechanical Engineering

ABSTRACT

Impact of Rotor Surface Velocity, Leakage Models and Real Gas Properties on Rotordynamic Force Predictions of Gas Labyrinth Seals. (May 2010)

Manish Rambhau Thorat, B.E., Mumbai University

Chair of Advisory Committee: Dr. Dara Childs

Rotordynamic coefficients of a gas labyrinth seal are assumed to be frequency independent. However, this assumption loses its validity as rotor surface velocity approaches Mach 1. The solution procedure of 1CV model by Childs & Scharrer which assumes frequency independent force coefficients is modified to allow for calculating frequency dependent force coefficients. A comparative study of the impact of using frequency-dependent model and the original frequency-independent model on stability analysis is made. The results indicate that frequency dependency of force coefficients should be accounted for in stability analysis as rotor surface velocity approaches a significant fraction of Mach number.

The bulk flow rotordynamic analysis model by Childs & Scharrer is modified to investigate the impact of leakage-flow models on predictions. A number of leakage models are incorporated in the one-control volume model, and a comparative study is made. Kinetic energy carryover factor of a leakage equation is one of the dominant factors in seal cross-force generation. A leakage equation based on a model proposed by

Gamal which uses Hodkinson's kinetic energy carryover factor is found to improve predictions of direct damping and cross-coupled stiffness.

A test case is implemented to study the impact of variation of seal axial radial clearance on stability characteristics.

The 1CV model by Childs & Scharrer and subsequent bulk flow models are based on the assumption of isothermal flow across the labyrinth seal. The 1CV model by Childs & Scharrer is modified to include energy equation, and the flow process is assumed to be adiabatic. However, predicted cross-coupled stiffness and direct damping coefficients using the new model do not compare well with the experimental results by Picardo as compared to the isothermal model. The impact of using real gas properties on static and rotordynamic characteristics of the seal is studied.

DEDICATION

Dedicated to my parents

ACKNOWLEDGEMENTS

I would like to express my sincere appreciation and gratitude to Dr. Dara Childs for his support and guidance. His exhaustive knowledge and insight in the field of rotordynamics has been a constant source of inspiration and has provided invaluable assistance during the course of research.

I am also greatly thankful to Dr. Morrison and Dr. Cizmas for serving on my committee.

Thanks also go to my friends and colleagues and the department faculty and staff for making my time at Texas A&M University a great experience. I also want to extend my gratitude to Turbomachinery Research Consortium for funding this research.

Finally, thanks to my parents and my sisters, Jyoti and Jyotsna, for their constant moral support and belief in me.

NOMENCLATURE

A	Cross-sectional area of control volume	[L^2]
B	Tooth height	[L]
b	Non-dimensional tooth height introduced in Eq. (31)	[-]
C, c	Direct and cross-coupled damping	[F t/L]
C_P	Specific heat at constant pressure	[FL/M T]
C_V	Specific heat at constant volume	[FL/M T]
Cr	Seal clearance	[L]
c_0	Speed of sound	[L/t]
f	Non-dimesional frequency in Eq. (31)	[-]
F_X,F_Y	Seal reaction forces	[F]
f_r, f_θ	Radial and circumferential dynamic stiffness coefficients	[F/L]
H	Seal clearance function	[L]
h	Enthalpy	[L^2/t^2]
$\tilde{h}$	Non-dimensional enthalpy introduced in Eq. (31)	[-]
$\tilde{h}_e$	Non-dimensional enthalpy coefficient introduced in Eq.(31)	[-]
j	$\sqrt{-1}$	[-]
K, k	Direct and cross-coupled stiffness	[F/L]
L	Pitch of seal strip	[L]
l	Non-dimensional pitch introduced in Eq. (31)	[-]
$\dot{m}$	Leakage flow rate	[M/L t]
$\tilde{\dot{m}}$	Non-dimensional leakage flow rate	[-]
P	Pressure	[F/ L^2]
P_e	Non-dimensional pressure coefficient introduced in Eq. (31)	[-]
p	Non-dimensional pressure introduced Eq.(31)	[-]

$\dot{Q}$	Heat flow rate	[F/t]
R	Gas constant	[L^2/T t^2]
R_S	Radius of Seal	[L]
Re	Reynolds' number	[-]
S	Entropy	[FL/T]
s	Complex variable for Laplace transform	[1/t]
T	Temperature	[T]
t	Time	[t]
$u_0(0)$	Preswirl ratio	[-]
$\hat{u}$	Specific internal energy	[L^2/t^2]
$\tilde{u}$	Non-dimensional specific internal energy introduced in Eq. (31)	[-]
V	Circumferential flow velocity	[L/t]
$\forall$	Volume	[L^3]
v	Non-dimensional circumferential velocity introduced in Eq. (31)	[-]
W	Axial flow velocity	[L/t]
$\dot{W}$	Power input/dissipation	[F/t]
X,Y	Relative displacement between stator and rotor	[L]
x, y	Non-dimensional relative displacement between stator and rotor	[-]
Z	Compressibility factor	[-]
γ	Ratio of specific heats	[-]
ε	Perturbation eccentricity ratio	[-]
θ	Circumferential coordinate	[-]
ξ	Non-dimensional radial clearance introduced in Eq. (31)	[-]
ρ	Density	[M/L^3]
$\tilde{\rho}$	Non-dimensional density introduced in Eq. (31)	[-]

$\tilde{\sigma}$	Non-dimensional parameter introduced in Eq. (31)	[-]
σ	Windage heating number introduced in Eq. (43)	[-]
τ	Non-dimensional time introduced in Eq. (31)	[-]
τ_r, τ_s	Shear stresses	[F/L^2]
$\tilde{\tau}_r, \tilde{\tau}_s$	Non-dimensional shear stresses introduced in Eq. (31)	[-]
λ_r, λ_s	Non-dimensional parameters introduced in Eq. (31)	[-]
ν	Kinematic viscosity	[L^2/t]
μ	Dynamic viscosity	[M/L t]
Ω	Excitation frequency	[1/t]
ω	Rotor speed	[1/t]
Π	Effective pressure ratio introduced in Eq.(44)	[-]

SUBSCRIPTS

0,1	Zeroth and first order
i	Seal cavity index
r,θ	Radial and circumferential
R,S	Rotor and stator

TABLE OF CONTENTS

CHAPTER Page

LIST OF FIGURES

FIGURE Page

FIGURE Page

LIST OF TABLES

CHAPTER I

INTRODUCTION

Labyrinth seals are used as sealing elements in turbomachinery applications such as compressors and turbines. They belong to a class of non-contacting seals to minimize leakage between a high-pressure and low pressure side. In centrifugal compressors, these seals are used as impeller eye seals, inter-stage seals, and balance piston seals. In turbines, they are typically employed to minimize blade-tip leakage. By minimizing secondary leakage losses in turbo-machines, labyrinth seals improve their efficiency. However, destabilizing forces developed in these seals can also be detrimental to the rotordynamic stability of these machines.

Labyrinth seal force-motion relationship is typically represented as:

$$-\begin{Bmatrix} F_X \\ F_Y \end{Bmatrix} = \begin{bmatrix} K & k \\ -k & K \end{bmatrix} \begin{Bmatrix} X \\ Y \end{Bmatrix} + \begin{bmatrix} C & c \\ -c & C \end{bmatrix} \begin{Bmatrix} \dot{X} \\ \dot{Y} \end{Bmatrix} \tag{1}$$

For gas labyrinth seals, inertia coefficients are negligible, and are neglected in conventional analysis.

Several analytical models have been proposed to model seal force generation. Alford [1], Kostyuk [2], Spurk & Keiper [3] developed simplified models to predict seal forces. However, these models require seal convergence/divergence to predict cross-forces. Iwatsubo [4] developed a comprehensive one control volume (1CV) model which considered the temporal variation of area, thus accounting for cross-forces for parallel displacement of rotor. Kurohashi et al. [5] developed a 1CV bulk flow model which included eccentricity-dependent flow coefficients. Childs & Scharrer [6] proposed a modification to the 1CV model which included angular area derivative in the continuity and momentum equations, previously neglected in analyses.

This thesis follows the style of Journal of Engineering for Gas Turbines and Power.

Wyssman et al. [7] developed a 2CV model which accounts for two distinct flow regimes in seal cavity- the vortex flow and the through-flow. Scharrer [8] provided an alternative 2CV model. Besides the development of bulk-flow models, Computational Fluid Dynamics (CFD) based approaches to solve the governing Navier-Stokes equations have been developed by Tam et al. [9], Nordmann and Dietzen [10], Rhode, Hensel and Guidry [11] and Athavale [12]. Moore [13] used a CFD method based on the approach by Athavale [12] and used experimental results on short gas labyrinth seals by Pelleti [14] to validate the predictions. Although CFD based methods take into account the entire flow physics of the domain, they are computationally expensive.

Wachter and Benckert [15] provide experimental results for statically offset labyrinth seals. The results confirm that seal rotordynamic coefficients are independent of eccentricity out to eccentricity of 0.5. The tests also confirmed the dependence of cross-coupled stiffness on inlet swirl. As the tests were conducted for static conditions, damping coefficients are not produced. Test results due to Wright [16] are available for single cavity convergent, divergent and constant clearance labyrinth seals. Childs & Scharrer [6] provide static and dynamic test results for both tooth-on-stator (TOS) and tooth-on-rotor (TOR) long labyrinth seals. Pelleti [14] provides test results for a short labyrinth seal. Picardo [17] tested a long TOS labyrinth seal for high pressure test cases.

Rotordynamic forces from a gas labyrinth seal are typically represented as frequency-independent stiffness and damping coefficients. Acoustic interaction in honeycomb gas seals is known to produce frequency dependent rotordynamic coefficients [18]. A similar acoustic interaction is possible in gas labyrinth seals due to standing waves in the circumferential annulus of the labyrinth seal. Frequency dependency of rotordynamic coefficients can be gauged experimentally by evaluating dynamic force coefficients. Wright [16] evaluated dynamic force coefficients at a single excitation frequency. The test shaft was precessed in a circular orbit at a frequency near the test rig's natural frequency. Kanemitsu and Ohasawa [19], and Millsaps & Martinez-Sanchez [20] used shaft-in-a-shaft test rig to evaluate force coefficients at different whirling speeds. Experimental results by Childs & Scharrer [6], Pelletti [14] and Picardo

[17] use external shakers to evaluate force coefficients at different excitation frequencies. As the range of excitation frequencies is small, Childs & Scharrer and Pelletti provide frequency independent rotordynamic coefficients evaluated by curve-fitting the dynamic force data. Data by Picardo [17] also shows frequency independent force coefficients up to excitation frequency of 150 Hz. The excitation frequencies considered by these researchers were much lower than the acoustic frequencies within the seal cavities.

Recent experimental investigation by Wagner et al. [21] on short stepped labyrinth seals clearly shows frequency dependency at higher excitation frequencies (range of excitation frequencies is -400 Hz to +400 Hz). Measured radial dynamic stiffness coefficients show a quadratic variation with excitation frequency, and circumferential dynamic stiffness coefficients show a linear variation. The quadratic frequency dependency of radial dynamic stiffness coefficients can be accounted for in rotordynamic analysis through the introduction of direct inertia terms in force-motion relations. However, the excitation frequencies considered in the tests were significantly lower than the acoustic frequency of the seal cavity.

In the present analysis, the 1CV model by Childs & Scharrer [6] is used as a base model to investigate the frequency dependency of rotordynamic coefficients. The original model employs a solution procedure which yields frequency-independent rotordynamic coefficients. One of the objectives of the present analysis is to implement a solution procedure by Thieleke & Stetter [22] which evaluates the rotordynamic coefficients as function of excitation frequency.

Comparison of bulk flow models with test results by Picardo [17] has not been satisfactory, with direct damping and cross-coupled stiffness coefficients significantly under-predicted. To develop an adequate model which yields better predictions, underlying physics behind the generation of seal forces is required. Using a simple 1CV model, Millsaps and Martinez-Sanchez [20] provide closed-form solutions for seal rotordynamic coefficients. Based on their hypothesis, Kinetic Energy (KE) carryover is a

dominant factor in the generation of cross-forces. The leakage equation is thus an important model element that needs to be considered.

Childs & Scharrer [6] 1CV bulk flow model uses a modified form of Neumann [23] leakage equation. The model neglects the eccentricity independency of KE carryover in the definition of first order perturbation constants used to derive rotordynamic coefficients. The 2CV model by Scharrer [8] uses an eccentricity-dependent KE carryover by Vermes [24]. However, comparisons of experimental data by Picardo [17] indicates that both models under-predict direct damping and cross-coupled stiffness. The above discrepancies clearly highlight the need for a leakage equation which yields good comparison with experimental results. Gamal [25] compares a number of leakage models with experimental leakage rates. Besides existing leakage models, Gamal [25] suggests several modified leakage models. These leakage models are compared with Picardo's experimental results in the present analysis.

Bulk flow models developed to date have considered the flow process in a labyrinth seal to be isothermal. A variation in temperature across the seal is expected due to rotor drag and kinetic energy carryover. Moreover in cases where the sealing fluid properties are far from ideal gas behavior, phenomenon such as Joule-Thomson effect can lead to large temperature variations across the seal. Estimation of windage heating loss is crucial to minimizing thermal losses in turbines/compressors. Experimental data on windage heating by McGreehan and Ko [26], Millwards and Edwards [27], Denecke et al. [28] are available for stepped labyrinth seals. There is a need for a comprehensive bulk flow rotordynamics model which takes into account temperature variation across the seal.

CHAPTER II

1CV BULK FLOW MODEL: FREQUENCY DEPENDENT ROTORDYNAMIC COEFFICIENTS

INTRODUCTION

The force motion relationship in Eq. (1) is valid only if the rotordynamic coefficients are frequency-independent. However, recent experimental investigations by Wagner, et al. [21] on stepped gas labyrinth seals have confirmed frequency-dependent force coefficients. Wagner et al. incorporate direct inertia terms in force-motion relationship to account for observed frequency dependency. However, these results do not consider high rotational speeds (rotor surface velocities approaching Mach 1) where the frequency-dependency may not be accounted for by inertia terms. In labyrinth seals, frequency dependency may arise due to the interaction of the excitation frequency with the fundamental acoustic frequency of the fluid in the annulus of seal. A similar acoustic interaction is known to produce frequency dependent coefficients in Honeycomb/hole-pattern seals [18]. To evaluate frequency dependency of rotordynamic coefficients, a 1CV model by Childs & Scharrer [6] is considered. However, solution procedure by Thieleke & Stetter [22] is used to obtain the rotordynamic coefficients.

ONE CONTROL VOLUME MODEL

Figures 1a and 1b show the schematic of the control volume. Continuity and circumferential momentum equations are derived for the model based on the analysis by Childs & Scharrer [6]. The flow is assumed to be isothermal.

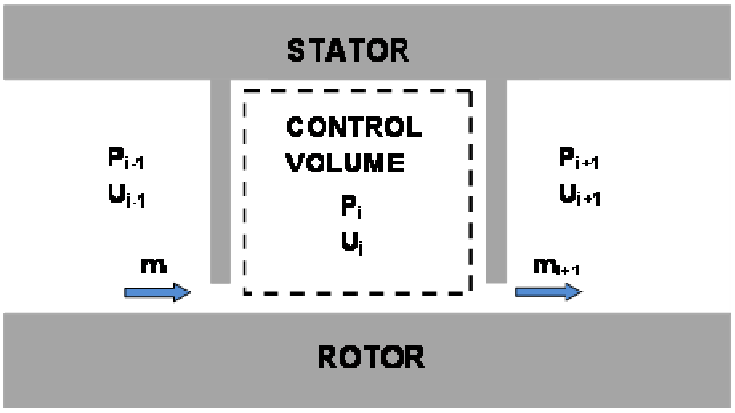

Figure 1a Axial view of control volume

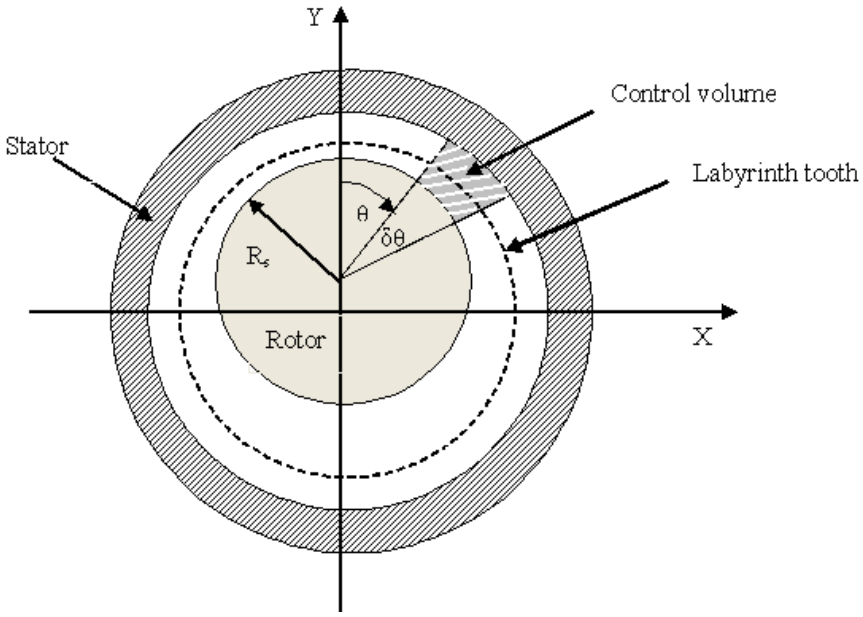

Figure 1b Radial view of the control volume

Continuity equation

$$\frac{\partial}{\partial\theta}\left(\frac{\rho_i A_i V_i}{R_s}\right)+\frac{\partial}{\partial t}(\rho_i A_i)+\dot{m}_{i+1}-\dot{m}_i=0 \qquad (2)$$

Circumferential momentum equation

$$\frac{\partial}{\partial\theta}\left(\frac{\rho_i A_i V_i^2}{R_s}\right)+\frac{\partial}{\partial t}(\rho_i A_i V_i)+\dot{m}_{i+1}V_i-\dot{m}_i V_{i-1}=-\frac{A_i}{R_s}\frac{\partial P_i}{\partial\theta}+(\tau_{Ri}a_{Ri}-\tau_{Si}a_{Si})L_i \qquad (3)$$

where a_R and a_S are dimensionless lengths upon which shear stress acts.

Rotor and stator shear stresses are modeled using a Blasius shear-stress model. To account for the curvature effects, the shear stress terms are modified according to Martinez-Sanchez et al. [29].

$$\tau_{Ri}=\tau_{Ri}\times(1.0+0.075(\frac{|R_s\omega-V_i|Dh_i}{\nu})^{0.25}\sqrt{\frac{Dh_i}{2R_s}})$$

$$\tau_{Si}=\tau_{Si}\times(1.0+0.075(\frac{|V_i|Dh_i}{\nu})^{0.25}\sqrt{\frac{Dh_i}{2R_s}})$$

where, Dh_i is the hydraulic diameter defined by

$$Dh_i=\frac{2(H_i+B_i)L_i}{(H_i+B_i+L_i)}$$

Leakage model

Neumann leakage model is used to model the axial leakage rate.

$$\dot{m}_i=\mu_{1i}\mu_2 H_i\sqrt{\frac{P_{i-1}{}^2-P_i^2}{RT}} \qquad (4)$$

Here, μ_{1i} is the flow coefficient by Chaplygin [30] and μ_2 is the kinetic energy carryover coefficient by Neumann [23].

Perturbation analysis

Perturbation analysis is used to solve the governing differential equations. Eccentricity ratio ε is used as the perturbation parameter, and the rotor is perturbed about a centered position. Zeroth-order solution of the differential equations yields steady

state leakage rates, pressure and velocity distribution in the seal cavities. The first-order solution yields perturbations in pressure and velocities within the seal cavities due to small fluctuations of the rotor about its centered position. Rotordynamic force coefficients are evaluated using pressure perturbations. Analysis by Millsaps and Martinez-Sanchez [20] indicates that force coefficients due to shear stress perturbations are negligible as compared to pressure perturbations; and hence they are neglected in the analysis.

The perturbed parameters are Pressure P_i, circumferential velocity V_i and the radial clearance H_i

$$P_i = P_{0i} + \varepsilon P_{1i}$$
$$V_i = V_{0i} + \varepsilon V_{1i}$$
$$H_i = Cr_{0i} + \varepsilon H_1$$

First order equations

First order continuity equation

$$G_{1i}\frac{\partial P_{1i}}{\partial t} + G_{2i}\frac{\partial P_{1i}}{\partial \theta} + G_{3i}\frac{\partial V_{1i}}{\partial \theta} + G_{6i}\frac{\partial H_1}{\partial t} + G_{7i}\frac{\partial H_1}{\partial \theta} + G_{8i}P_{1i} + G_{9i}P_{1i-1} + G_{10i}P_{1i+1} + G_{13i}H_1 = 0 \quad (5)$$

First order circumferential momentum equation

$$X_{1i}\frac{\partial P_{1i}}{\partial t} + X_{2i}\frac{\partial P_{1i}}{\partial \theta} + X_{3i}\frac{\partial V_{1i}}{\partial t} + X_{4i}\frac{\partial V_{1i}}{\partial \theta} + X_{7i}\frac{\partial H_1}{\partial t} + X_{8i}\frac{\partial H_1}{\partial \theta} + X_{9i}P_{1i} + X_{10i}P_{1i-1} + X_{11i}P_{1i+1} + X_{12i}V_{1i} + X_{13i}V_{1i-1} + X_{16i}H_1 = 0 \quad (6)$$

The coefficients G_{1i} and X_{1i} are defined in appendix A.

SOLUTION PROCEDURE

Equation 1 represents a form of force-motion relationship if the rotordynamic force coefficients are assumed to be frequency independent. To solve for the four rotordynamic coefficients *K, k, C* and *c*, a minimum of 4 equations are required. 1CV analysis by Childs & Scharrer assumes an elliptical orbit for rotor whirl as depicted in Fig. 2. An elliptical orbit can be decomposed into a forward and backward circular whirl orbits as shown in Fig. 3. Thus, by assuming an elliptical orbit, four equations are obtained corresponding to the two whirl frequencies, which can be solved for the four coefficients. The rotor is assumed to be whirling at the rotor speed.

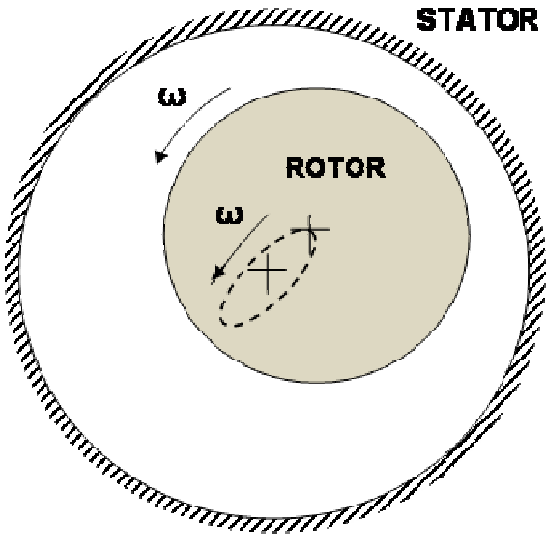

Figure 2 Elliptical orbit

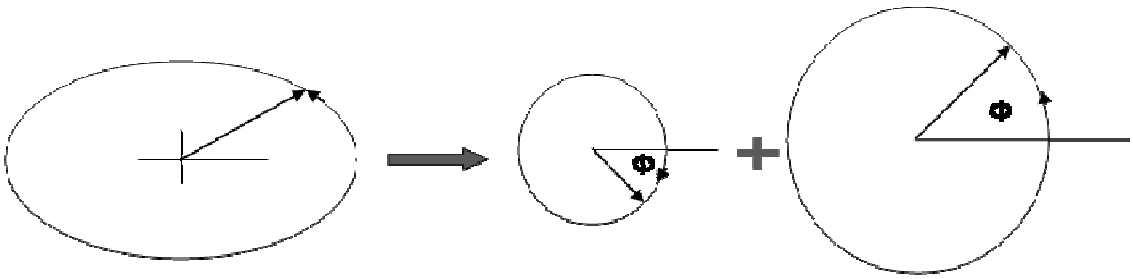

Figure 3 Elliptical orbit decomposed into forward and backward whirl orbits

The elliptical orbit solution is valid only if the rotordynamic coefficients are frequency independent. Another approach to evaluate rotordynamic coefficients is through the use of circular whirl orbit for rotor perturbation. Childs & Kim [31] use this approach to evaluate force coefficients of a liquid annular seal. Thieleke and Stetter [22] follow this method for evaluating frequency independent force coefficients for a gas labyrinth seal. Figure 4 shows the schematic of a circular whirl orbit and Eq. (7) represents the form of the solution:

$$X = a\cos\Omega t, Y = a\sin\Omega t \tag{7}$$

Substituting in Eq.(1) yields

$$\begin{aligned} F_X &= -Ka\cos\Omega t + ca\Omega\sin\Omega t \\ F_Y &= ka\cos\Omega t - Ca\Omega\sin\Omega t \end{aligned} \tag{8}$$

Resolving the force components into radial and circumferential terms:

$$\begin{aligned} \frac{F_r}{a} &= f_r = -(K + c\Omega) \\ \frac{F_\theta}{a} &= f_\theta = k - C\Omega \end{aligned} \tag{9}$$

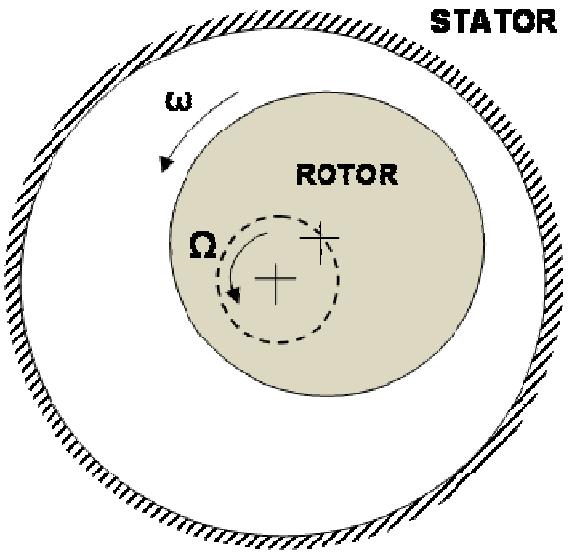

Figure 4 Schematic of rotor rotating at speed ω and whirling in a circular orbit at frequency Ω

Equation 9 represents two equations and four unknowns. Therefore a minimum of two frequencies is required to evaluate the coefficients. For more than two frequencies, the force coefficients are obtained by curve fitting. To analyze the frequency dependency, the dynamic force coefficients $f_r(\Omega)$ and $f_\theta(\Omega)$ are evaluated for a range of excitation frequencies. If $f_r(\Omega)$ and $f_\theta(\Omega)$ do not vary linearly with Ω as indicated by Eq.(9) , the force coefficients are frequency dependent.

FREQUENCY DEPENDENCY AND ACOUSTIC INTERACTION

1CV analysis by Childs & Scharrer and subsequent bulk flow models assume that the lowest acoustic frequency within the circular annulus of the seal is much higher than the rotor speed. The frequency independent model of Eq. (1) breaks down if the rotor speed approaches the lowest cavity acoustic frequency. Figure 5 shows a schematic of various acoustic modes within the circular annulus of labyrinth seal cavity.

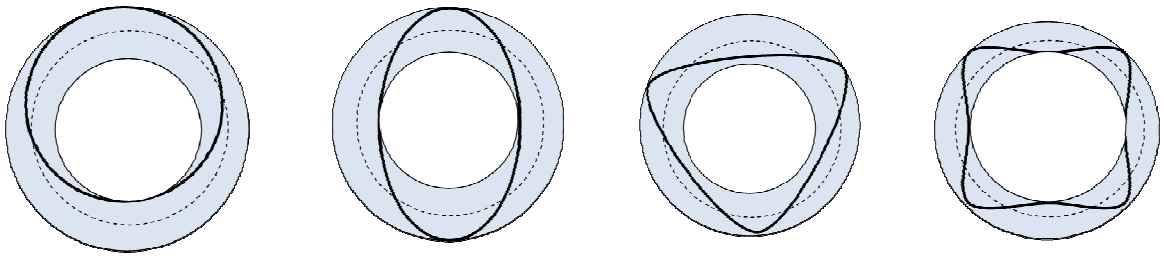

Figure 5 Acoustic modes in a labyrinth seal cavity

The fundamental acoustic frequency is obtained by considering the circular annulus to be an open-ended pipe as depicted in Fig. 6. Neglecting the flow velocity within the pipe and enforcing continuity at the pipe ends yield a simplified form of natural frequencies:

$$\omega_{ni}(pipe) = \frac{i\pi c_0}{L} \Rightarrow \omega_{ni}(cavity) = \frac{2i\pi c_0}{2\pi R_s} = \frac{ic_0}{R_s}; i = 1, 2, \ldots \tag{10}$$

where, c_0 is the isothermal speed of sound and R_s is the seal radius.

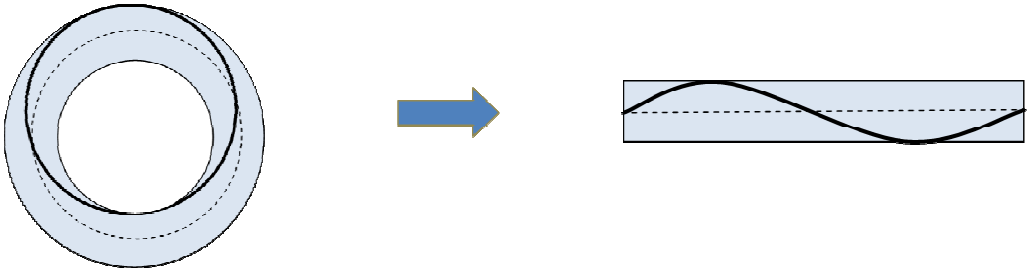

Figure 6 Fundamental acoustic mode: Evaluation of acoustic frequency

The rotor speed equal to the first acoustic frequency is:

$$\omega = \omega_{n1} = \frac{c_0}{R_s} \Rightarrow R_s\omega = c_0 \tag{11}$$

The limiting condition for rotor speed approaching the 1st acoustic frequency is the same as the rotor surface velocity approaching the acoustic velocity, c_0.

To analyze frequency dependency, a test case of a long labyrinth seal is considered. Seal geometry and operating conditions are obtained from experimental set-up of Picardo [17]. Table 1 provides the input data.

Table 1: Seal geometry and operating conditions by Picardo

Reservoir Pressure	70 bar
Sump Pressure	36 bar
Temperature	288 K
Radial Clearance	0.198 mm
Seal Radius	57.340 mm
Tooth Pitch	4.293 mm
Tooth Height	4.293 mm
Rotor Friction Constant	0.079
Rotor Friction Exponent	-0.250
Stator Friction Constant	0.079
Stator Friction Exponent	-0.250
Compressibility Factor	1.000
Ratio of Specific Heats	1.400
Kinematic Viscosity	0.00001510 m^2/s
Gas Constant	286.900 J/kg K
Number of Teeth	20
Tooth Location	Stator

Figures 7a and 7b show the variation of $f_r(\Omega)$ and $f_\theta(\Omega)$ versus rotor excitation frequency for a rotor speed of 15.2krpm. The excitation frequency is non-dimensionalized with respect to the rotor speed. The plots clearly indicate the resonance peaks of the 1st acoustic frequency. As the rotor speed ω increases, the dynamic force coefficients at the rotor speed are strongly influenced by resonance. The linear expressions of Eq. (9) can no longer be used to define f_r and f_θ .

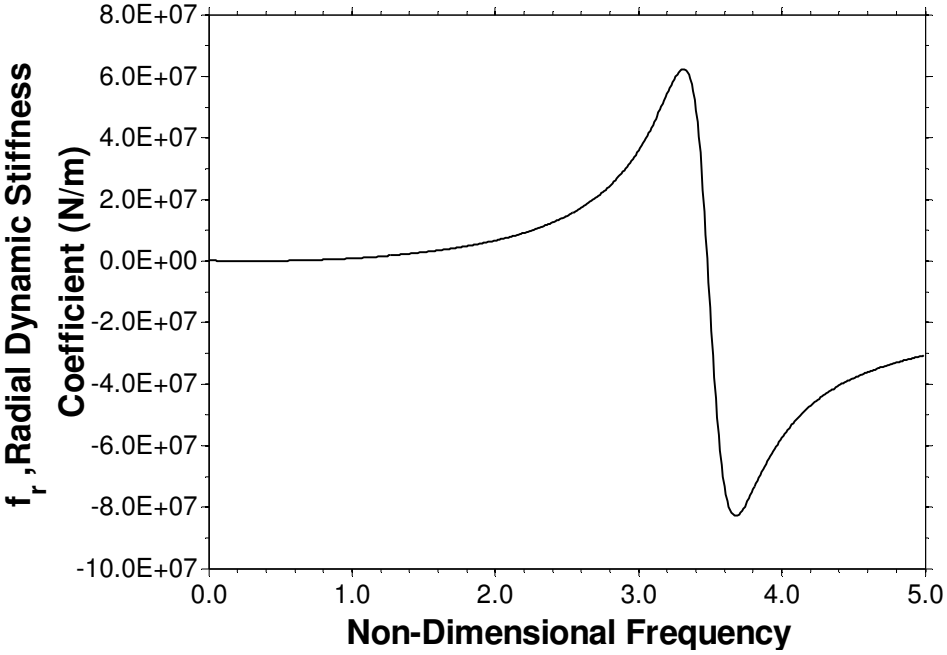

Figure 7a Radial dynamic stiffness coefficient versus excitation frequency, (Preswirl ratio=0)

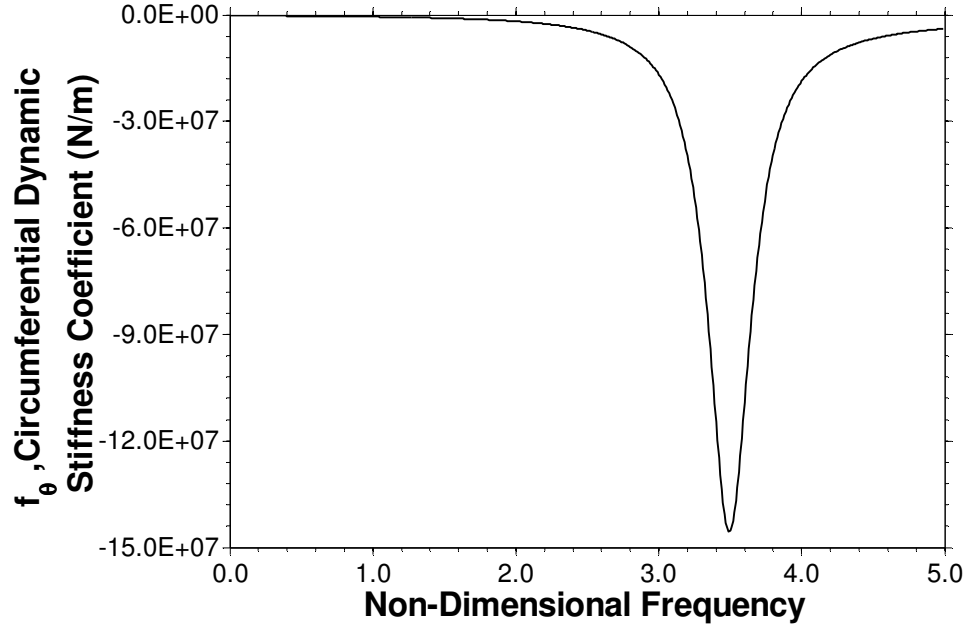

Figure 7b Circumferential dynamic stiffness coefficient versus excitation frequency, (Preswirl ratio=0)

The resonant frequency in the plots of f_r and f_θ is slightly higher than the acoustic frequency evaluated using Eq.(10). This discrepancy can be attributed to: (a) circumferential flow velocity becomes an appreciable fraction of c_0 and (b) convective acceleration terms are retained in the model that are neglected in conventional acoustics.

TRANSFER FUNCTION MODEL AND FREQUENCY DEPENDENT ROTORDYNAMIC COEFFICIENTS

If $R_s\omega$ approaches c_0, f_r and f_θ cannot be modeled by the frequency-independent model of Eq. (9). A similar situation arises in honeycomb/hole-pattern stator seals where the apparent acoustic velocity for flow within the seal can be reduced due to the effect of gas compressibility within the holes/cells, dropping the lowest acoustic frequency into the operating region. Kleynhans and Childs [18] present solutions that produce frequency-dependent rotordynamic coefficients for these types of seals, following the approach of Bolleter et al. [32]. Their transfer-function model is

$$-\begin{Bmatrix} F_X(s) \\ F_Y(s) \end{Bmatrix} = \begin{bmatrix} \boldsymbol{D}(s) & \boldsymbol{E}(s) \\ -\boldsymbol{E}(s) & \boldsymbol{D}(s) \end{bmatrix} \begin{Bmatrix} x(s) \\ y(s) \end{Bmatrix} \tag{12}$$

with $\boldsymbol{D}$ and $\boldsymbol{E}$ defined as follows:

$$\begin{aligned} f_r^{+}(\Omega) &= -\mathrm{Re}[\boldsymbol{D}(\boldsymbol{j}\Omega)] - \mathrm{Im}[\boldsymbol{E}(\boldsymbol{j}\Omega)] \\ f_r^{-}(\Omega) &= -\mathrm{Re}[\boldsymbol{D}(\boldsymbol{j}\Omega)] + \mathrm{Im}[\boldsymbol{E}(\boldsymbol{j}\Omega)] \\ f_\theta^{+}(\Omega) &= +\mathrm{Re}[\boldsymbol{E}(\boldsymbol{j}\Omega)] - \mathrm{Im}[\boldsymbol{D}(\boldsymbol{j}\Omega)] \\ f_\theta^{-}(\Omega) &= +\mathrm{Re}[\boldsymbol{E}(\boldsymbol{j}\Omega)] + \mathrm{Im}[\boldsymbol{D}(\boldsymbol{j}\Omega)] \end{aligned} \tag{13}$$

Here, the '+' superscript indicates positive precession motion and '-' superscript indicates negative precession motion. The complex functions $\boldsymbol{D}(\boldsymbol{j}\Omega)$ and $\boldsymbol{E}(\boldsymbol{j}\Omega)$ are obtained by adding and subtracting terms in Eq.(13).

Analytical expressions are obtained for $\boldsymbol{D}$ and $\boldsymbol{E}$ by curve-fitting to standard polynomial forms. Figures 8 and 9 provide representative results for ω = 15200 rpm and zero-preswirl.

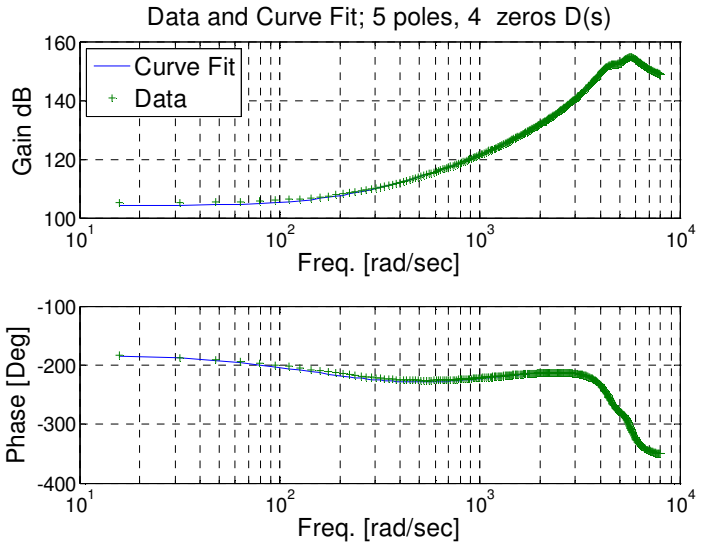

Figure 8 Magnitude and Phase plot of calculated and curve-fitted D transfer function (Zero preswirl, rotor speed 15200 RPM)

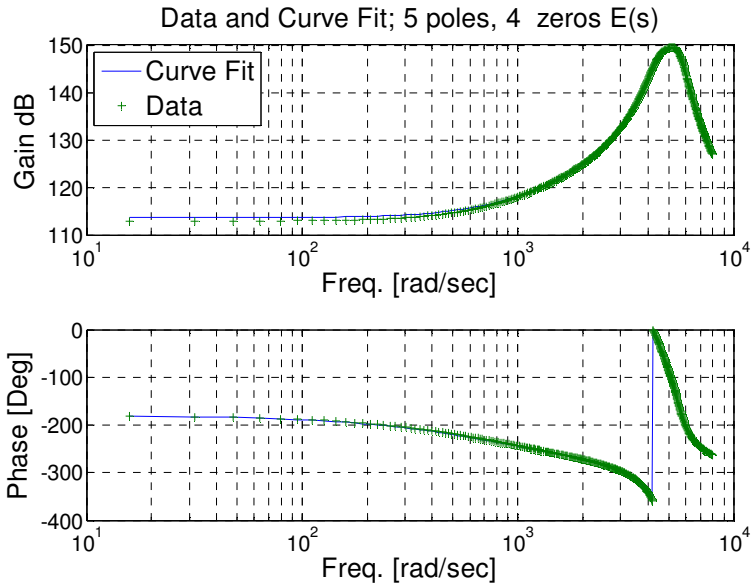

Figure 9 Magnitude and Phase plot of calculated and curve-fitted E transfer function (zero pre-swirl, rotor speed 15200 RPM)

JEFFCOTT ROTOR MODEL- IMBALANCE RESPONSE AND STABILITY ANALYSIS

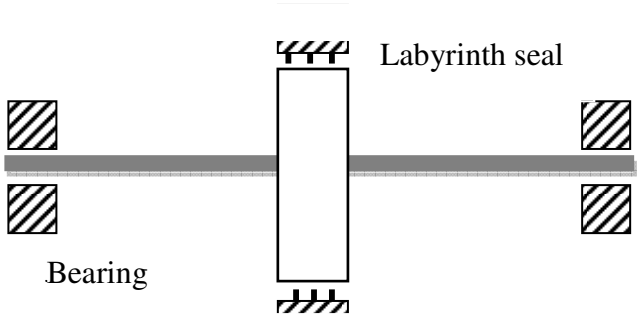

Figure 10 Simple Jeffcott rotor

The Jeffcott rotor model of Fig. 10, acted on by labyrinth seal forces is used to consider the effect of frequency dependency on synchronous response and stability analysis.

The rotor parameters are:

Mass (m)	100 kg
Naturalfrequency, $\omega_{nr} = \sqrt{\frac{k_r}{m}}$	795.87 rad/sec = 7.6 krpm

This natural frequency is half the rotor speed of 15.2 krpm. This choice was made to amplify any possible impact of the labyrinth on rotor stability. The labyrinth seal parameters used here are shown in Table 1. Labyrinth seal forces are the only source of stabilizing or destabilizing forces in the model.

Imbalance-response calculations

The governing equation for the Jeffcott rotor model of Fig. 10 with conventional labyrinth seal forces is:

$$\begin{bmatrix} m & 0 \\ 0 & m \end{bmatrix} \begin{Bmatrix} \ddot{x} \\ \ddot{y} \end{Bmatrix} + \begin{bmatrix} C & c \\ -c & C \end{bmatrix} \begin{Bmatrix} \dot{x} \\ \dot{y} \end{Bmatrix} + \begin{bmatrix} K + k_r & k \\ -k & K + k_r \end{bmatrix} \begin{Bmatrix} x \\ y \end{Bmatrix} = \begin{Bmatrix} me\omega^2 \cos \omega t \\ me\omega^2 \sin \omega t \end{Bmatrix} \tag{14}$$

Here, k_r is the rotor stiffness and e is the rotor imbalance.

Comparisons were made for the speed-dependent (frequency-independent) model and the frequency and speed dependent model for a range of inlet swirl ratios and rotor speeds. Figure 11 shows the (same) calculated *synchronous* amplitude results for both models. Although not shown, the *synchronous* phase plots also coincide. Synchronous-response predictions coincide for the two models because the rotordynamic coefficients are calculated for forward precession at ω for both model types.

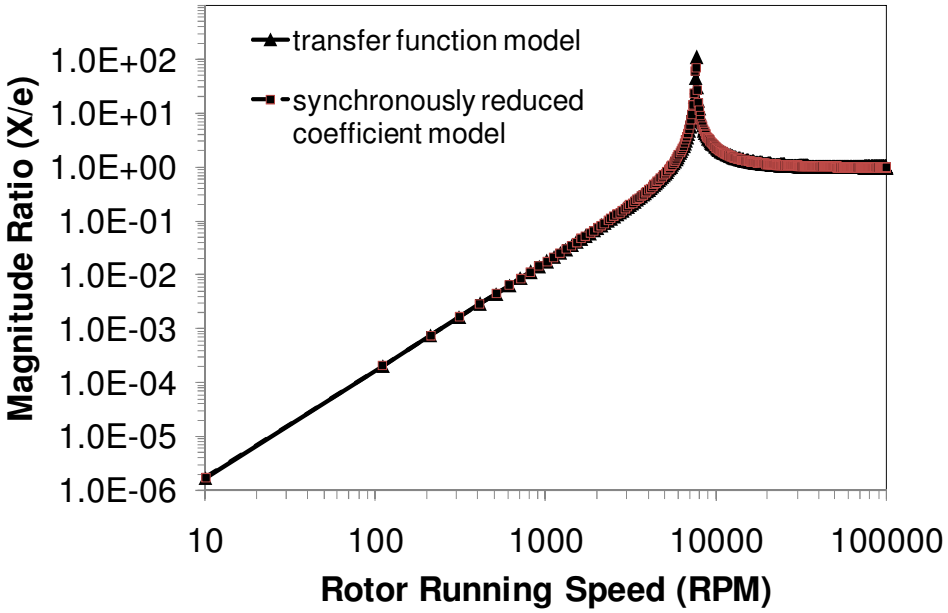

Figure 11 Magnitude plot for frequency-independent model (synchronously reduced coefficients) and frequency dependent model (Transfer function model) for $u_0(0) = 0.5$

Stability calculations

Speed-dependent, frequency-independent model approach

The frequency-independent model is implemented considering synchronously-reduced rotordynamic coefficients evaluated using elliptical precessional orbit at the rotor running speed. The homogeneous version of Eq. (14) applies.

Frequency-dependent models

Frequency dependency can be accounted by using Eq. (1) *with frequency dependent* rotordynamic coefficients, with the corresponding precession frequencies equal to the rotor's damped natural frequencies. A similar approach is sometimes used to account for the *calculated* frequency dependency of tilting-pad bearings. Thus, the rotordynamic coefficients for forward and backward damped natural frequencies can be extracted from the *D* and *E* transfer functions via:

$$\begin{aligned} K &= \mathrm{Re}[\boldsymbol{D}(j\omega_{dnr})] \\ k &= \mathrm{Re}[\boldsymbol{E}(j\omega_{dnr})] \\ C &= \frac{\mathrm{Im}[\boldsymbol{D}(j\omega_{dnr})]}{\omega_{dnr}} \\ c &= \frac{\mathrm{Im}[\boldsymbol{E}(j\omega_{dnr})]}{\omega_{dnr}} \end{aligned} \tag{15}$$

where, $\boldsymbol{\omega_{dnr}}$ is the damped natural frequency of the rotor.

For hole-pattern stator seals, seal forces can significantly change the damped natural frequencies of the rotor. In such cases, the rotordynamic coefficients are re-evaluated at the calculated damped natural frequencies, and the procedure is repeated until there is convergence between the assumed and calculated natural frequency. Thus, the stability analysis becomes iterative in nature. However, labyrinth seal forces do not significantly change the rotor's damped natural frequencies. The stability analysis including a labyrinth seal would be non-iterative.

The second frequency-dependent approach involves directly implementing the *D* and *E* transfer-function results into the rotor model using a state-space format.

Figures 12-14 present calculated log-dec results for the model versus the inlet preswirl ratio $u_0(0)$, which is varied from 0 to 0.8. Zero corresponds to a highly-effective swirl brake, and 0.8 corresponds to a high preswirl value to be expected for a balance-piston seal with no swirl brake. Results were obtained using the following three approaches:

- Speed dependent, frequency-independent model.
- Frequency-dependent stiffness and damping coefficients.
- *D* and *E* transfer-function model.

Results are only presented for forward -precessing modes.

Test case 1: ω = 15.2 krpm; $R_s\omega = 0.26\, c_0$

Figure 12 shows the following outcomes:

- The synchronously reduced model predicts instability at a pre-swirl ratio of ~0.35.
- The frequency-dependent model predicts instability at a pre-swirl ratio of ~0.42.
- The transfer-function model predicts instability at a preswirl ratio of ~0.43.

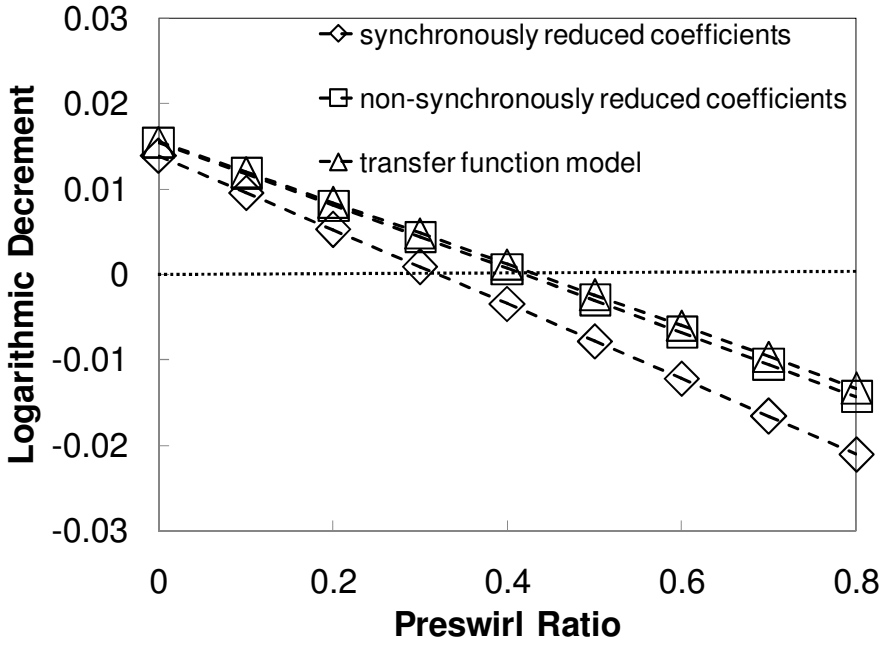

Figure 12 Log-dec versus $u_0(0)$ (ω = 15.2 krpm)

Test case 2: ω = 40 krpm; $R_s\omega = 0.7c_0$

Figure 13 shows the following outcomes:

- The synchronously-reduced model predicts instability at all preswirl ratios up to 0.8.
- The frequency-dependent and transfer-function models predicts instability at a preswirl ratio greater than ~ 0.22.

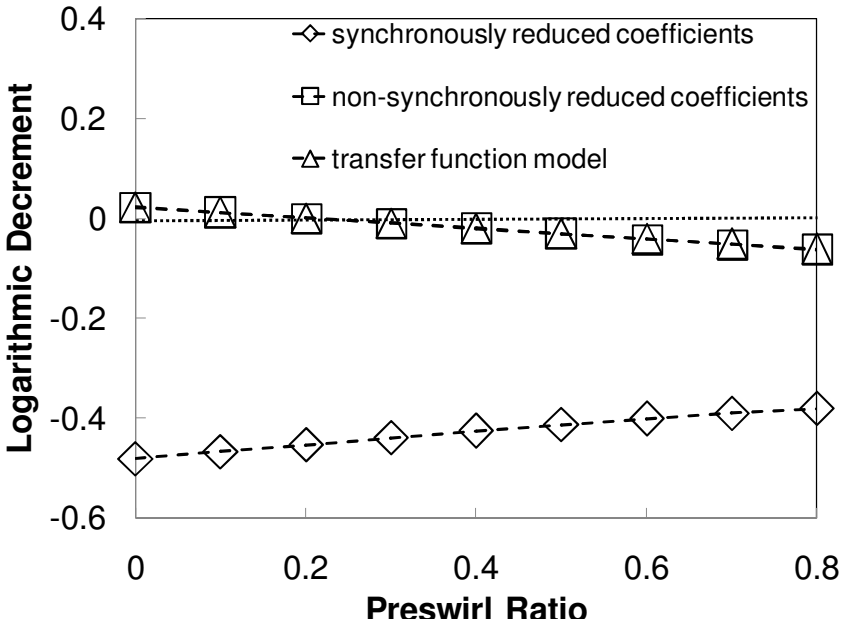

Figure 13 Log-dec versus $u_0(0)$ (ω = 40 krpm)

Test case 3: ω = 70 krpm; $R_s\omega = 1.2c_0$

Figure 14 illustrates the following outcomes:

- The synchronously-reduced model predicts stability for $0 \leq u_0(0) \leq 0.8$.
- The frequency-dependent model and the transfer function model predict instability for $0 \leq u_0(0) \leq 0.8$.

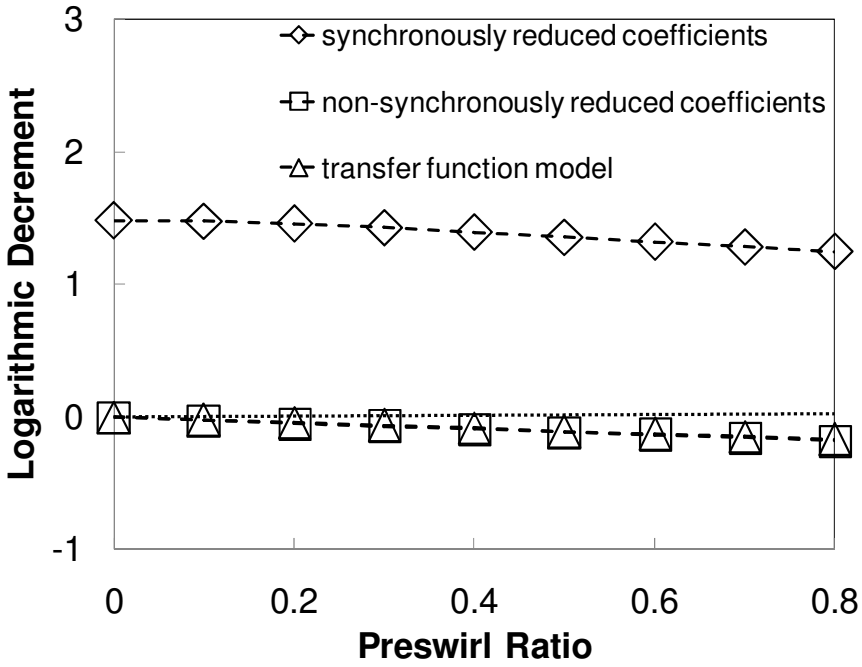

Figure 14 Log-dec versus $u_0(0)$ (ω = 70 krpm)

Evaluation of onset speed of instability

The onset speeds of instability for forward precessing mode are evaluated for $u_0(0)$=0.5. Figure 15 illustrates the predicted log dec, showing that stability calculations are about the same for synchronously-reduced and frequency-dependent solution up to ~14 krpm, but diverge from this speed onwards. The frequency-dependent model predicts an onset speed of instability of 10 krpm.

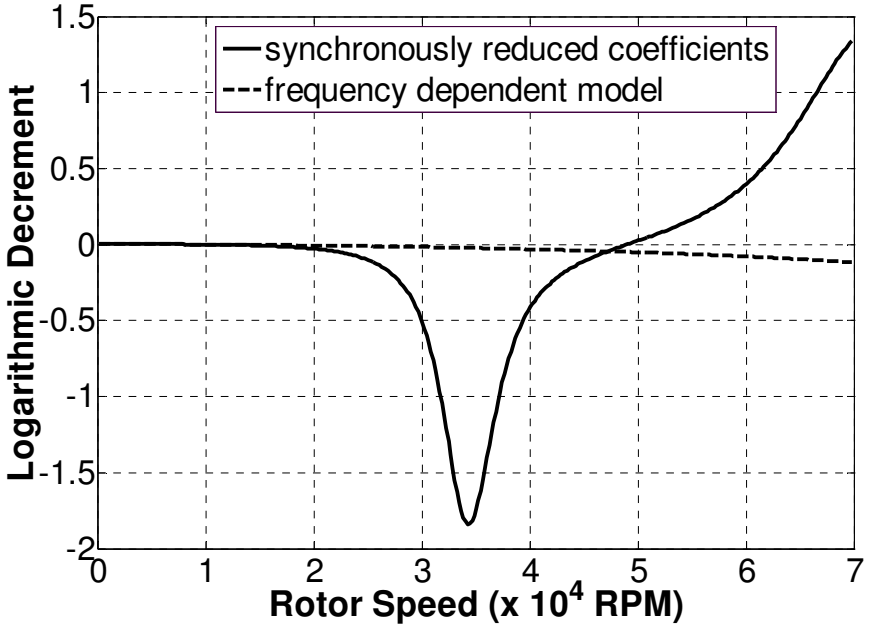

Figure 15 Log-dec versus rotor speed

The historical experience with labyrinth seals is that they produce low values of direct stiffness and have a minimal impact on the rotor natural frequencies. Figure 16 shows the calculated damped natural frequency for the rotor's forward precession mode. The synchronously-reduced model shows it first dropping and then increasing sharply as the ω increases. The frequency-dependent results show a modest drop in the natural frequency with increasing ω. A comparison of Figs. 15 and 16 suggests that differences between the log-dec predictions for the models arise mainly due to erroneous predictions of the damped natural frequency for the synchronously-reduced model; i.e., that is predictions of direct stiffness terms that simply do not exist.

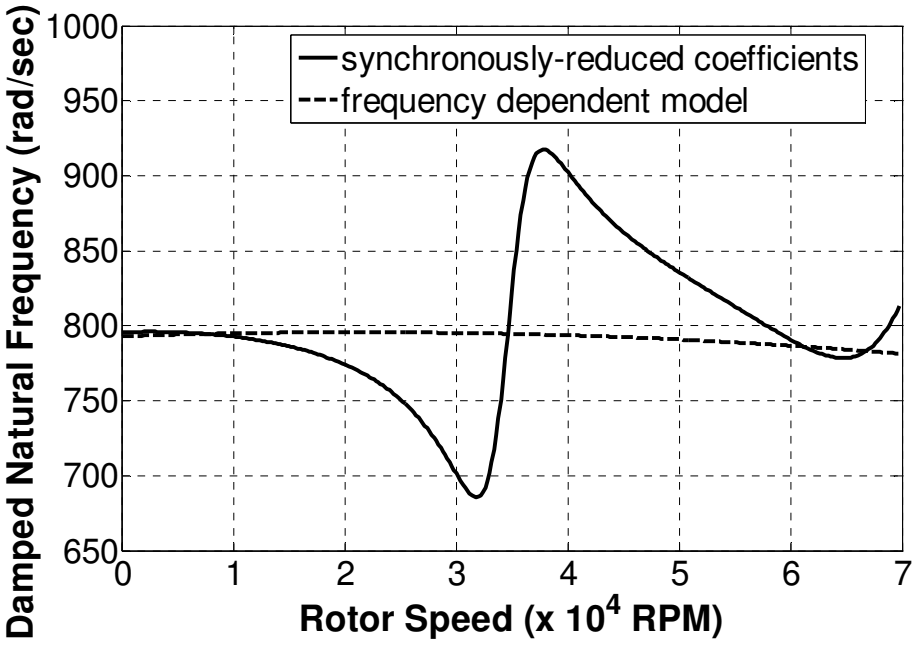

Figure 16 Damped natural frequencies versus rotor speed

The stability analysis clearly indicates that as rotor surface velocity approaches a significant fraction of Mach 1, the rotordynamic coefficients become strongly frequency dependent. The test cases considers an impractical rotor speed (>~40krpm) where the effects of frequency dependency are significant, note that the test case is considered for air which has a high acoustic speed. For some hydrocarbons such as propane, the acoustic velocity can be significantly lower, causing much lower rotor speeds to show frequency dependency.

CHAPTER III

PARAMETRIC STUDY OF BULK FLOW MODEL: INFLUENCE OF LEAKAGE EQUATION

Axial flow in a labyrinth seal is complex and characterized by the presence of recirculation zones with a step pressure difference across teeth instead of a gradual drop in pressure. To model the flow, bulk-flow models for labyrinth seals employ empirical/semi-empirical leakage flow models instead of axial momentum equation in the governing equations. Some uncertainties in the prediction of rotordynamic coefficients arise from the uncertainties in modeling the leakage flow. The 1CV bulk flow model by Childs and Scharrer [6] employs a modified form of semi-empirical leakage equation by Neumann [23] to estimate the leakage loss. The 2CV bulk flow model by Scharrer [8] uses a Neumann leakage model based on Vermes [24] kinetic energy carryover coefficient. The present analysis aims to improve the predictions and gauge the possible impact of leakage flow on seal rotordynamics.

CLOSED FORM SOLUTION FOR 1CV MODEL

Millsaps and Martinez-Sanchez [20] provide closed-form solution for rotordynamic forces based on a 1CV model for a single cavity labyrinth seal. The closed form solutions indicate that the cross-force coefficients (direct damping & cross-coupled stiffness) are proportional to $K-(1-\frac{1}{\alpha})$; where K represents the variation of Kinetic energy carryover with radial displacement and α represents the ratio of exit to inlet radial clearance.

Based on 1CV model by Childs & Scharrer [6], the term $K-(1-\frac{1}{\alpha})$ corresponds to the change in derivative of mass-flow rate as the flow proceeds from inlet to exit of the control volume.

$$K-(1-\frac{1}{\alpha})=\frac{C_{ri}}{\dot{m}_0}(\frac{\partial \dot{m}_{i+1}}{\partial H_{i+1}}-\frac{\partial \dot{m}_i}{\partial H_i}) \tag{16}$$

where, C_{ri} is the inlet radial clearance to the cavity, H_i is the radial clearance as a function of radial displacement and time.

Equation (16) clearly highlights the dependence of direct damping and cross-coupled stiffness on leakage rate. Note that the dependence of leakage rate on radial clearance is an important factor influencing the coefficients. The K.E. carryover factor as a function of radial clearance is an important parameter which needs to be considered in the selection of adequate leakage equation for a labyrinth seal.

LEAKAGE MODELS

Estimation of leakage loss through a labyrinth seal has been a subject of numerous investigations. Gamal [25] summarizes the leakage models developed by Martin [33], Egli [34], Hodkinson [35], Vermes [24] and several others. In addition to the existing leakage flow models, Gamal [25] suggested five modified leakage models which are termed as MOD (1-5). Gamal's models are applicable to a single tooth of the labyrinth. An iterative procedure is required to evaluate leakage for a multi-tooth labyrinth seal. The leakage equations proposed are based on two base models: (a) St. Venant Equation and (b) Neumann leakage. Equation (17) illustrates St. Venant Equation and Eq. (18) represents Neumann base leakage model,

$$\dot{m}_i=\frac{A_i P_{i-1}}{\sqrt{\gamma R T_{i-1}}}\sqrt{\frac{2\gamma^2}{\gamma-1}\left(\left(\frac{P_i}{P_{i-1}}\right)^{\frac{2}{\gamma}}-\left(\frac{P_i}{P_{i-1}}\right)^{\frac{\gamma+1}{\gamma}}\right)} \tag{17}$$

$$\dot{m}_i=A_i\sqrt{\frac{P_{i-1}{}^2-P_i^2}{RT_{i-1}}} \tag{18}$$

The models proposed by Gamal are based on combining different flow-coefficients and K.E. carryover with the two base models. Chaplygin's [30] flow

coefficient and the constant flow coefficient of 0.716 by Eser & Kazakia [36] are considered in the leakage models.

Chaplygin's flow coefficient is a function of pressure ratio across the restriction and is represented by:

$$\mu_{1i} = \frac{\pi}{\pi + 2 - 5S_i + 2S_i^2}, S_i = \left(\frac{P_{i-1}}{P_i}\right)^{\frac{\gamma-1}{\gamma}} - 1 \tag{19}$$

Table 2 provides the definition of K.E. carryover coefficients.

Table 2: K.E. carryover factor definitions

Vermes	$\mu_{2i} = \sqrt{\frac{1}{1-\alpha_i}}, \alpha_i = \frac{8.52}{\frac{(L_i - t_i)}{C_{ri}} + 7.23}$ Where, L_i = tooth pitch of seal t_i = tooth thickness C_{ri} = radial clearance
Neumann	$\mu_{2i} = \sqrt{\frac{NT}{(NT-1)j + j}}, j = 1 - \left(1 + 16.6\frac{C_{ri}}{L_i}\right)^{-2}$ Where, NT = number of teeth
Hodkinson	$\mu_{2i} = \sqrt{\frac{1}{1 - \left(\frac{NT-1}{NT}\right) \cdot \left(\frac{C_{ri}/L_i}{(C_{ri}/L_i) + 0.02}\right)}}$

Table 3 summarizes the models which are considered for comparison in the present analysis.

Table 3: Leakage models

Leakage Model	Base Model	K.E. carryover	Flow coefficient
Neumann	Neumann	Neumann	Chaplygin
Scharrer	Neumann	Vermes	Chaplygin
MOD1	St. Venant	Hodkinson	None
MOD2	St. Venant	Vermes	None
MOD3	St. Venant	Vermes	Chaplygin
MOD4	Neumann	Vermes	None
MOD5	St. Venant	Hodkinson	Chaplygin
Gamal model	St. Venant	Hodkinson	Eser & Kazakia

PERFORMANCE OF LEAKAGE MODELS

Comparison of leakage rates

Gamal [25] provides a comparison of leakage rates for the proposed models based on experimental results by Picardo [17]. A similar comparison is made in the present section with the addition of leakage rate comparison for Gamal leakage model. Table 4 shows the test conditions for long labyrinth seals (no. of teeth = 20) tested by Picardo [17]. The seal type A corresponds to 0.2 mm radial clearance and type B corresponds to 0.1 mm radial clearance.

Table 4: Seal geometry and test conditions by Picardo [13]

Seal Type/Test Case	Swirl-Ratio	Inlet Pressure (bar)	Exit Pressure (bar)	Rotational Speed (rpm)	Seal Clearance (mm)	Leakage rate (kg/s)
A1	-0.098	71.06	11.99	10227	0.2	0.449
A2	-0.099	70.17	25.08	10225	0.2	0.443
A3	-0.098	72.06	37.93	10208	0.2	0.407
B1	0.074	70.74	7.21	10214	0.1	0.232
B2	0.071	70.35	21.65	10216	0.1	0.227
B3	0.082	69.82	36.01	10213	0.1	0.204

Table 5 which provides comparison of percentage error of the leakage models indicates that for high pressure labyrinth seals, MOD2 and MOD4 leakage equations accurately predict leakage rates (<10%). Gamal leakage models yields reasonable predictions for 0.2 mm clearance. The Neumann leakage model shows a maximum prediction error of ~66%. As stated earlier, 1CV model by Childs & Scharrer employs Neumann leakage equation to account for axial leakage. The justification for a new leakage model arises from this discrepancy.

Table 5: Percentage errors for leakage models versus Picardo's data

Leakage model	A1	A2	A3	B1	B2	B3
Neumann	-14.1	-17.7	-18.5	-26.8	-66.1	-28.8
Scharrer	-37.0	-39.6	-40.2	-40.0	-41.4	-42.3
MOD1	23.0	24.4	24.4	12.2	14.1	14.1
MOD2	-4.8	-4.1	-4.0	-8.9	-7.4	-7.3
MOD3	-39.0	-40.6	-40.8	-41.3	-42.5	-42.8
MOD4	-4.8	-2.6	-3.1	-8.9	-5.7	-6.5
MOD5	-19.8	-22.7	-23.2	-26.6	-28.8	-29.6
Gamal Model	-8.8	-10.7	-10.5	-17.3	-18.1	-18.0

Table 6 provides the test labyrinth seal geometry for low-pressure labyrinth tested by Gamal [25]. The seal considered is a tooth-on-stator type labyrinth seal. Inlet pressures are in the range of 100 psi-a (6.89 bar) to 35 psi-a (2.49 bar). The back pressure is kept constant at atmospheric pressure.

Table 6: Labyrinth seal geometry tested by Gamal

Seal Pitch	12.7 mm
Seal radius	50.9 mm
Cavity depth	12.7 mm
Number of Teeth	4
Radial clearance	0.102 mm

The low pressure test results of Gamal in Fig. 17 suggest that leakage models Mod3 and Scharrer models perform well as compared to other models. The Gamal leakage model shows high prediction error (~40%) for inlet pressure of 35 psi-a. However as the inlet pressure increases, the prediction error decreases with the best leakage prediction for 100 psi-a inlet pressure. Thus, Gamal leakage model performs well under both high pressure and low pressure conditions.

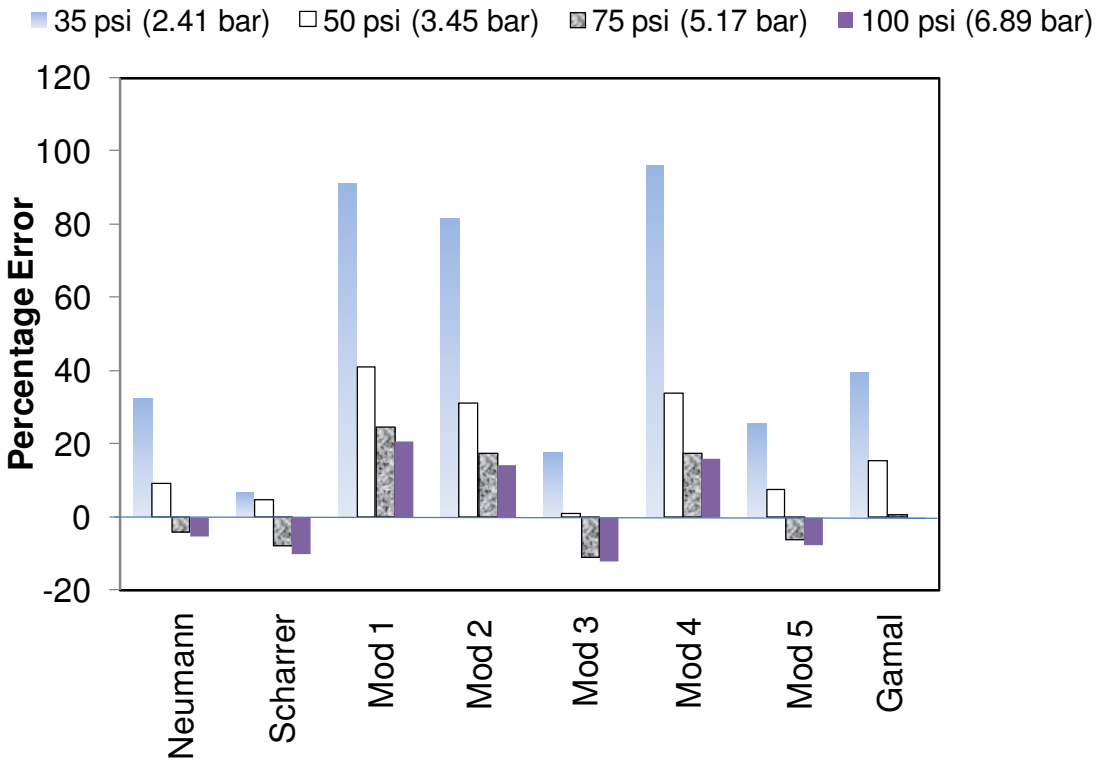

Figure 17 Prediction errors of different leakage models for Gamal test seal

Comparison of rotordynamic coefficients

1CV model developed by Childs & Scharrer [6] to evaluate rotordynamic coefficients is modified to consider the different leakage models proposed in the

previous section. Experimental results by Picardo [17] are used as a basis to compare the predictions based on these leakage models.

Note that the 1CV model by Childs & Scharrer [6] ignores the derivative of K.E. carryover in the definition of first order coefficients of perturbation which are used to obtain force coefficients. The present analysis includes this term in the model. Table 1 provides the seal geometry tested by Picardo [17]. Air is used as the sealing fluid in the tests.

For a labyrinth seal, cross-coupled stiffness and direct damping are extremely important in determining the stability of a rotordynamic system. The direct stiffness and cross-coupled damping are generally insignificant in altering the stability characteristics of a rotordynamic system; hence, they are not considered for comparison in the present analysis.

Figure 18a shows the impact of considering derivative of K.E. carryover term on predictions of cross-coupled stiffness. The plot clearly affirms Millsaps hypothesis that a significant fraction of cross-coupled stiffness is contributed by the derivative of KE carryover. The model considering KE carryover yields better predictions when compared to experimental results. Figure 18b which compares direct damping also confirms the predictions of Millsaps.

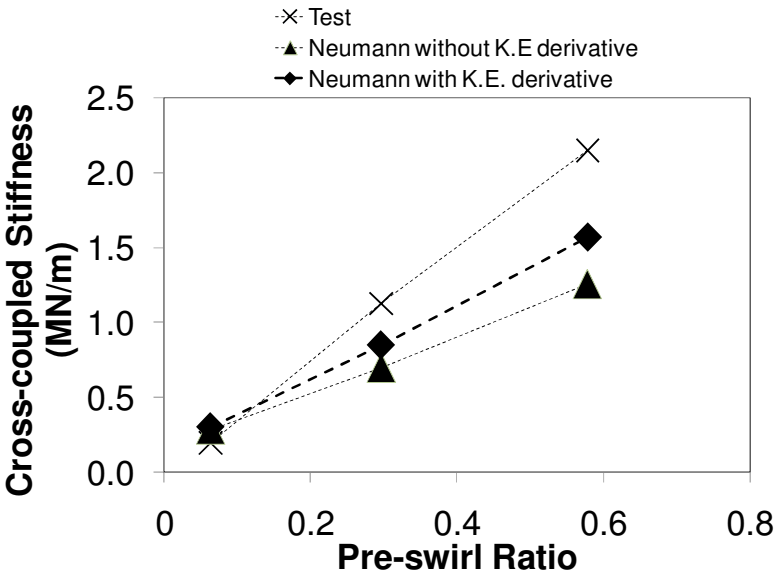

Figure 18a Comparison of cross-coupled stiffness test results with predictions based on Neumann leakage model with and without KE carryover derivative

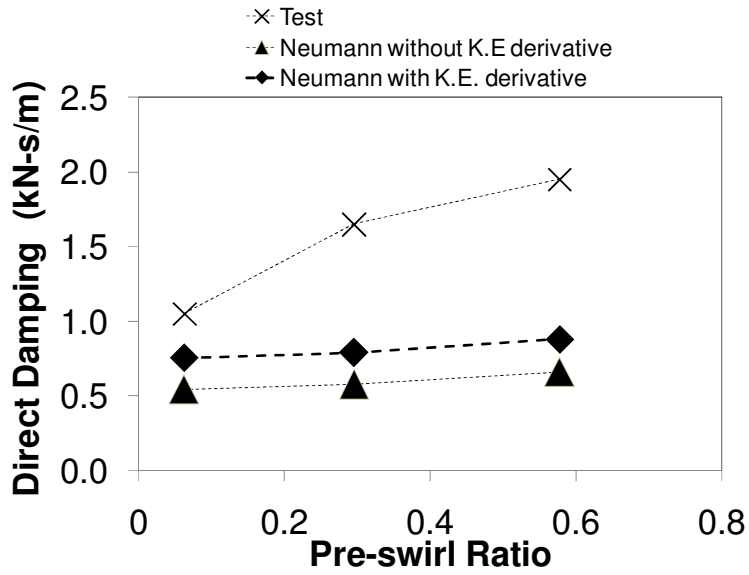

Figure 18b Comparison of direct damping test results with predictions based on Neumann leakage model with and without KE carryover derivative

Figure 19 depicts the variation of cross-coupled stiffness with preswirl and rotor speed for the seal with 0.2 mm radial clearance. The figure indicates that MOD1 leakage equation performs the best, followed by Gamal leakage model and Neumann leakage model. The Scharrer leakage model performs the worst in predicting cross-coupled stiffness.

Comparison of direct damping coefficients as depicted in Fig. 20 also shows a similar trend as obtained for cross-coupled stiffness.

Although Mod1, Gamal leakage equation and Neumann equation show improvement over other models, the improvement is marginal as compared to the experimental values. As the rotor speed increases, the calculated damping coefficients approach experimental values.

Of all the models considered for comparison, Mod1 leakage model yields best predictions for cross-force coefficients. However, the leakage rates predicted by this model do not compare well with experimental results. The Gamal leakage model shows reasonably accurate leakage predictions for both high and low pressure test cases as well gives better results for rotordynamic coefficients as compared to other models. *Thus, the Gamal leakage equation represents a suitable alternative for bulk flow models.*

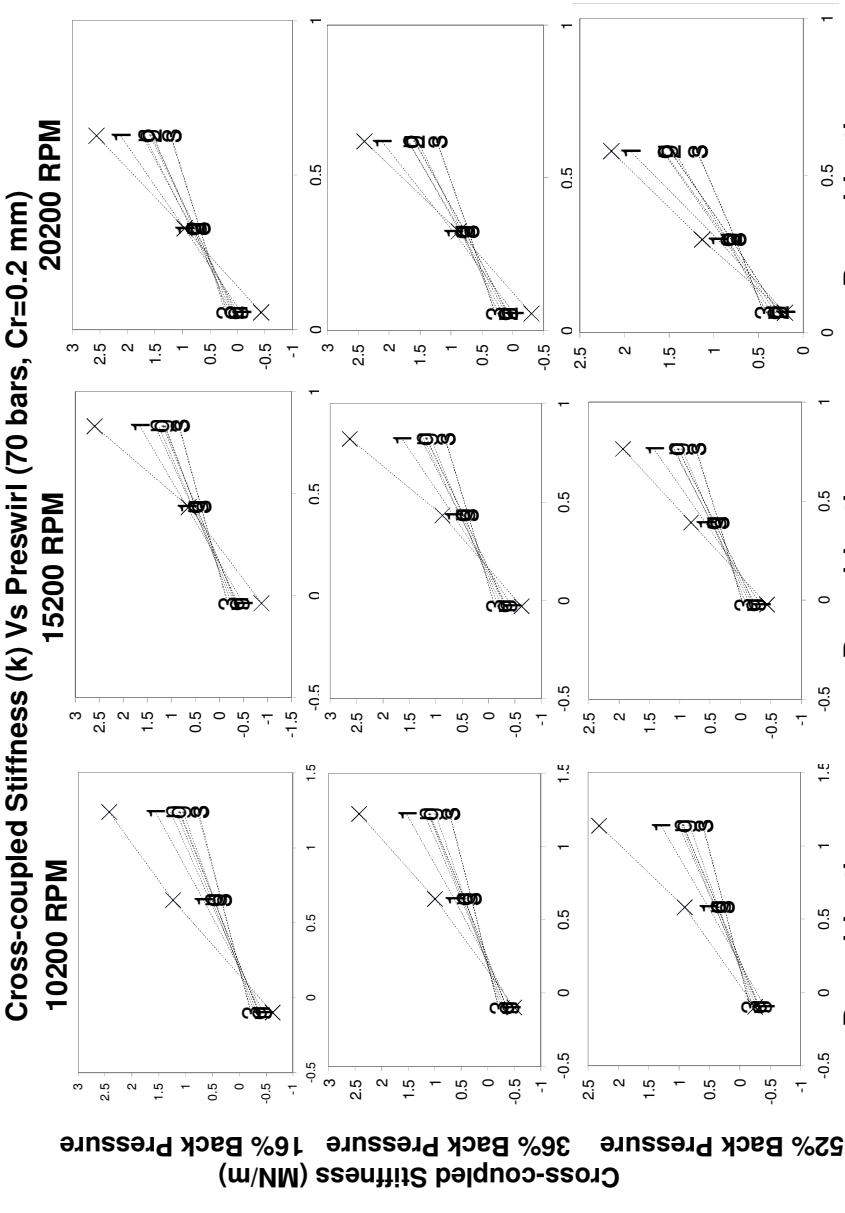

Figure 19 Cross-coupled stiffness predictions from different leakage models versus experimental results

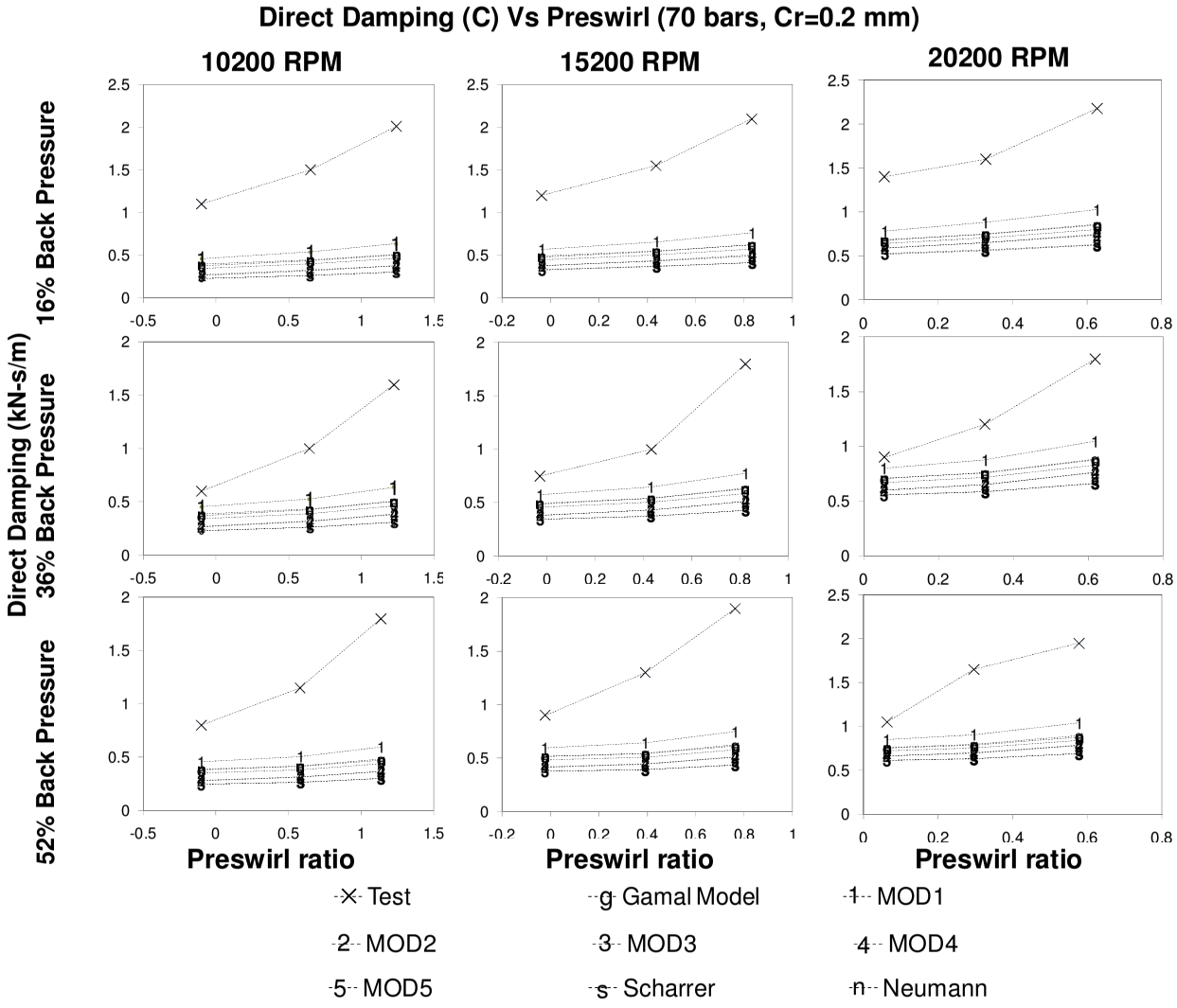

Figure 20 Direct damping predictions from different leakage models versus experimental results

CHAPTER IV

1CV BULK FLOW MODEL: IMPACT OF SEAL CONVERGENCE/ DIVERGENCE ON PREDICTIONS

INTRODUCTION

The seal clearance at the impeller eye of a centrifugal compressor can vary due to seal distortion attributed to thermal or centrifugal stresses. The present analysis aims to investigate the effect of variation in seal clearance on the stability characteristics of a labyrinth seal.

Development of analytical model for labyrinth seal force generation started with the assumption of varying inlet-to-outlet radial clearance for axial flow only. Alford [1] developed one of the first models to explain the generation of Labyrinth seal forces. Alford's model attributed the generation of destabilizing forces to the axial variation of seal radial clearance. Alford's theory predicts positive direct damping for diverging clearance, and negative for converging clearance. However, this theory neglects the circumferential flow within the seal cavities and does not predict cross-coupled forces for constant clearance. Spurk and Keiper [3], provide analytical predictions for a single cavity labyrinth with results contrary to that obtained by Alford [1].

Wright [16] describes test results for single-cavity labyrinth seals with constant, converging and diverging radial clearances. The test results indicate that converging seals are more stable than diverging seals. Gans [37] also considers the effect of varying clearances on the stability of rotor systems. Predictions based on his analysis indicate that as the clearance is made more converging, the destabilizing force tends to increase for forward whirl. Kurohashi [5] developed an analytical model for labyrinth seal and conducted experimental investigation on labyrinth seals with constant, converging and diverging clearances, in a non-rotating test rig. The test results for damping however indicate a trend which is exactly opposite to that proposed by Alford [1] and Gans [37]. Experimental investigations by Vance, et al. [38] indicated negative effective damping

for all seal configurations (uniform, diverging and converging radial clearances) for the given test conditions. However, the negative damping was found to be less for diverging seal clearances as compared to converging clearances, thus qualitatively conforming to the original analysis by Alford. Note that preswirl was not measured by Vance, et al. [38]. Zero inlet swirl was assumed as the flow was supplied to the labyrinth through straight vanes. The measured results would then correspond to effective damping.

SEAL GEOMETRY AND OPERATING CONDITIONS

Figure 21 shows the schematic of Labyrinth seal configurations considered in the analysis. The axial variation of tip clearance considered for converging and diverging configurations is linear.

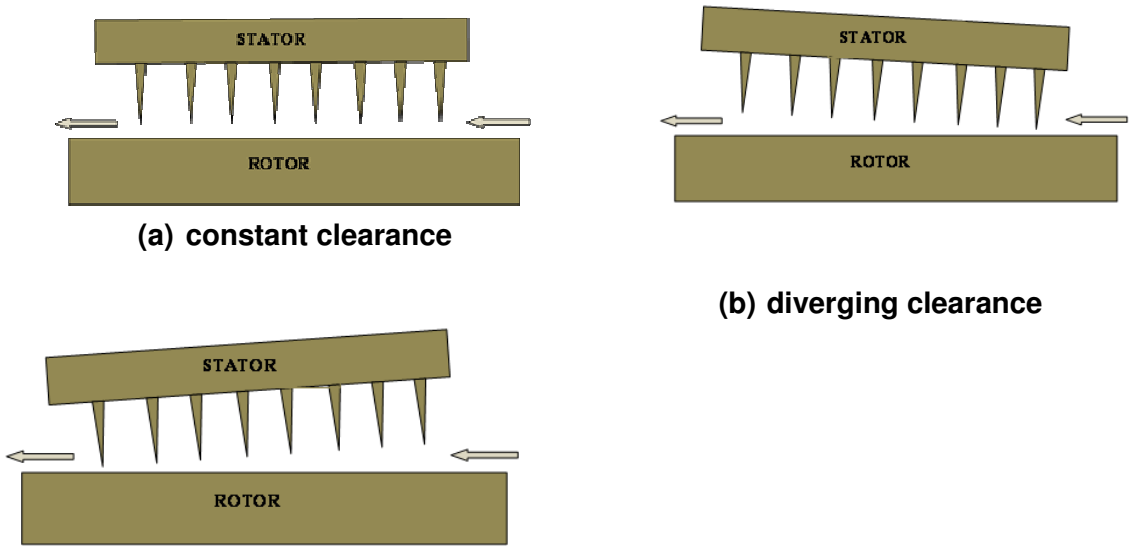

Figure 21 Schematic of Labyrinth seal (TOS) with a) constant b) diverging and c) converging clearance

To consider the effect of variation in seal clearance a test case of Picardo [17] is considered in the analysis. The experimental investigation by Picardo considers only constant clearances. The present analysis includes test cases with radial clearance that is converging as well as diverging along the seal length. The seal average clearance is kept constant. Tables (7-8) provide seal dimensions and operating conditions for the present analysis.

Table 7: Seal dimensions (in mm)

Dimension	Straight	Converging/Diverging
Radius	57.34	57.34
Tooth height	4.293	4.293
Tooth pitch	4.293	4.293
Radial clearance	0.2	0.1-0.3
Number of Teeth	20	20

Table 8: Operating conditions

Reservoir Pressure	70 bar
Sump Pressure	36 bar
Temperature	288 K

STATIC CHARACTERISTICS

Static characteristics of a seal correspond to the pressure distribution and leakage rate. Although, the average seal clearance is kept constant, table 9 indicates that converging/diverging seals leak less compared to the seal with constant clearance. The disparity in leakage rates is the least between the converging and diverging seal types.

Table 9: Leakage rates [kg/s]

constant clearance	0.393
diverging clearance	0.319
converging clearance	0.322

Figure 22 shows the pressure distribution for the three types of seal configurations considered. The diverging clearance shows a large pressure drop in the first few seal cavities as compared to the other two types of seals considered.

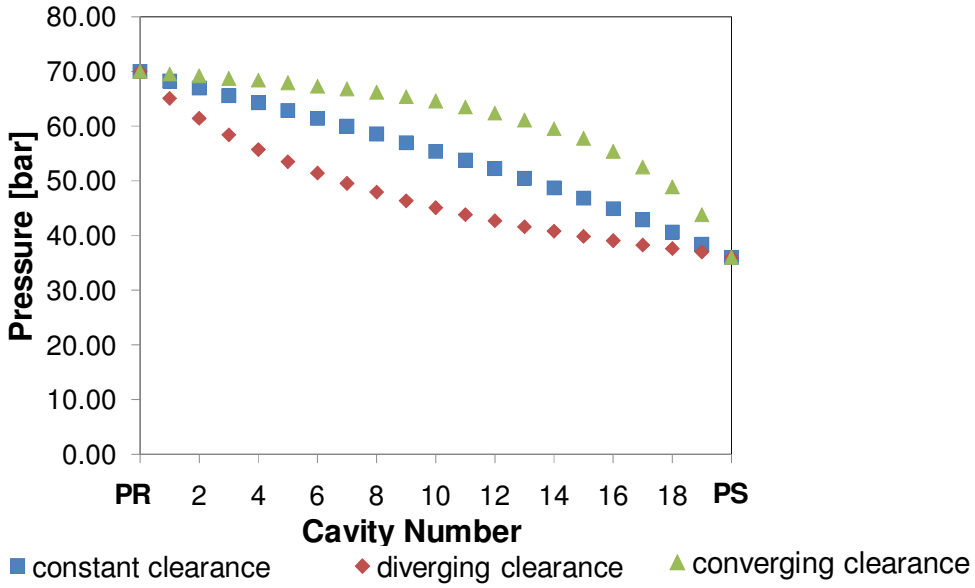

Figure 22 Pressure distribution in seal cavities for constant, diverging and converging seal clearances

STABILITY CHARACTERISTICS

Figure 23 compares direct damping, cross-coupled stiffness and effective damping for the three seal configurations. The direct damping is fairly constant over the

range of pre-swirl ratios considered and is highest for converging clearance. This is contrary to Alford's [1] hypothesis which proposes that direct damping is higher for diverging clearance. Cross-coupled stiffness is highest for the converging seal type. Cross-coupled stiffness increases with increase in pre-swirl which reaffirms the sensitivity of cross-coupled stiffness to inlet swirl. The plot of effective damping indicates that a converging seal would yield a more stable configuration.

Closed-form solutions developed by Millsaps and Martinez-Sanchez [20] indicate that a diverging clearance seal would be stabilizing if the, ratio of excitation frequency (Ω) to angular velocity of swirl within the seal cavity, Γ, is less than 1. Similarly, a converging clearance labyrinth seal would be stabilizing if Γ is greater than 1. Considering excitation frequency to be equal to rotor speed ($\Omega=\omega$), the ratio Γ is always greater than 1.Thus, 1CV model with synchronously reduced coefficients for a diverging clearance labyrinth would always predict destabilizing forces for forward whirl and a converging clearance would always predict stabilizing forces.

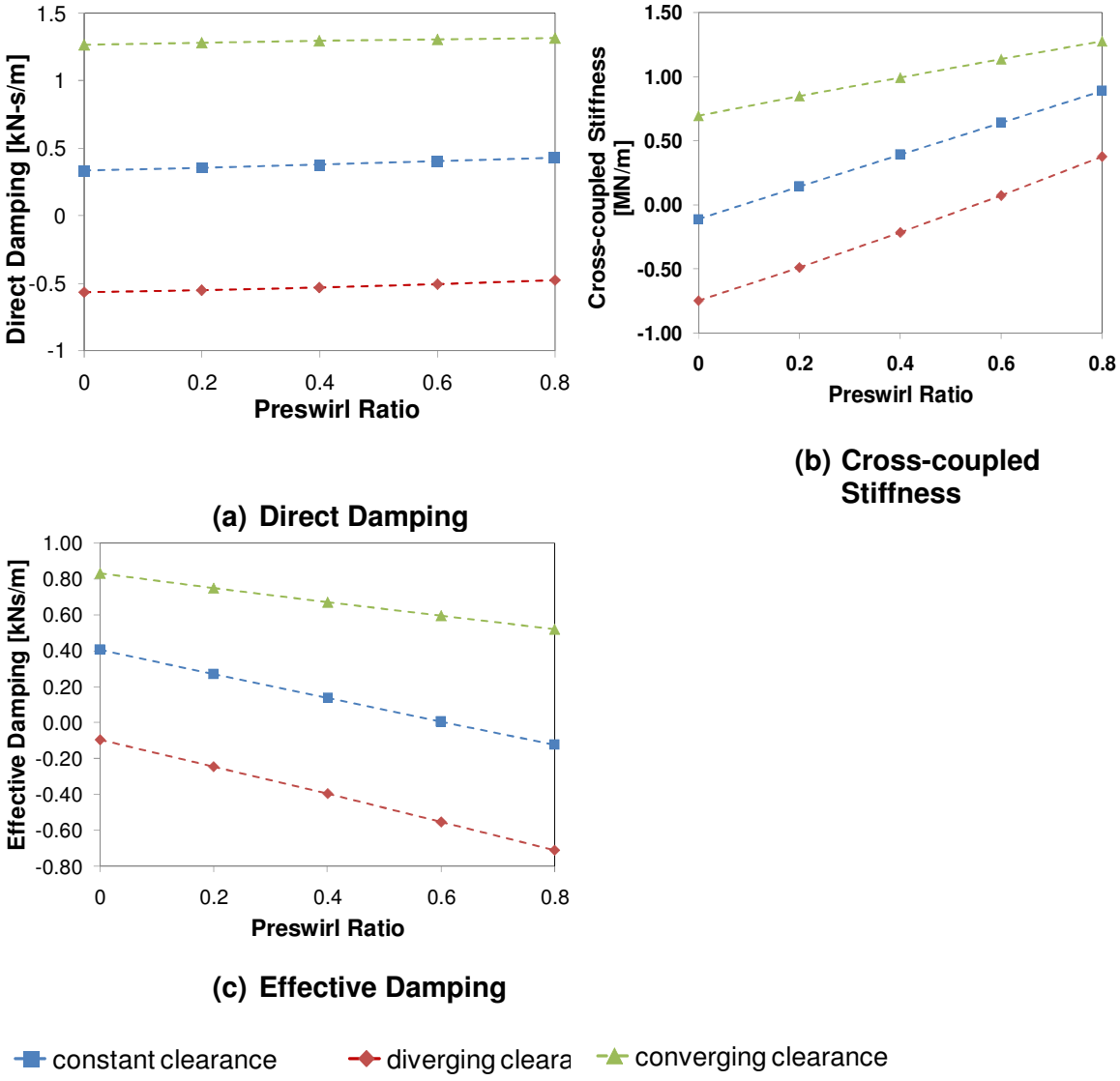

Figure 23 Comparison of variation with preswirl of (a) Direct damping (b) Cross-coupled stiffness and (c) Effective damping for constant (0.2 mm radial clearance), diverging (0.1 mm-0.3 mm radial clearance) and converging clearance (0.3mm-0.1mm radial clearance)

Figures 24 and 25 show effective damping plotted for a range of excitation frequencies at a rotor speed of 10 krpm at two different preswirl ratios. The excitation frequencies are non-dimensionalized with respect to the rotor speed. The seal geometry and test conditions of Table 7 and 8 are considered in the analysis. Effective damping is

indicative of the stability characteristics of the seal. The plots indicate the well-known sensitivity of cross-forces in a labyrinth seal to preswirl ratios. For a preswirl ratio of 0.5, the converging clearance labyrinth would be unstable for excitation frequency less than ~0.4 times rotor speed. The diverging clearance is stable for all excitation frequencies up to rotor speed for zero preswirl and unstable for all excitation frequencies for 0.5 preswirl. Note that all the three configurations show similar behavior at non-dimensional excitation frequencies around 0.3-0.4. The labyrinth seal considered in this case is a tooth-on-stator labyrinth and the average swirl velocity is around 0.3 times rotor speed. The ratio Γ is approximately equal to 1 at the excitation frequency corresponding to 0.3 times rotor speed. The plots confirm Millsaps & Martinez-Sanchez hypothesis for a long labyrinth seal that a converging clearance labyrinth would be destabilizing for Γ <1 and stabilizing for Γ >1.

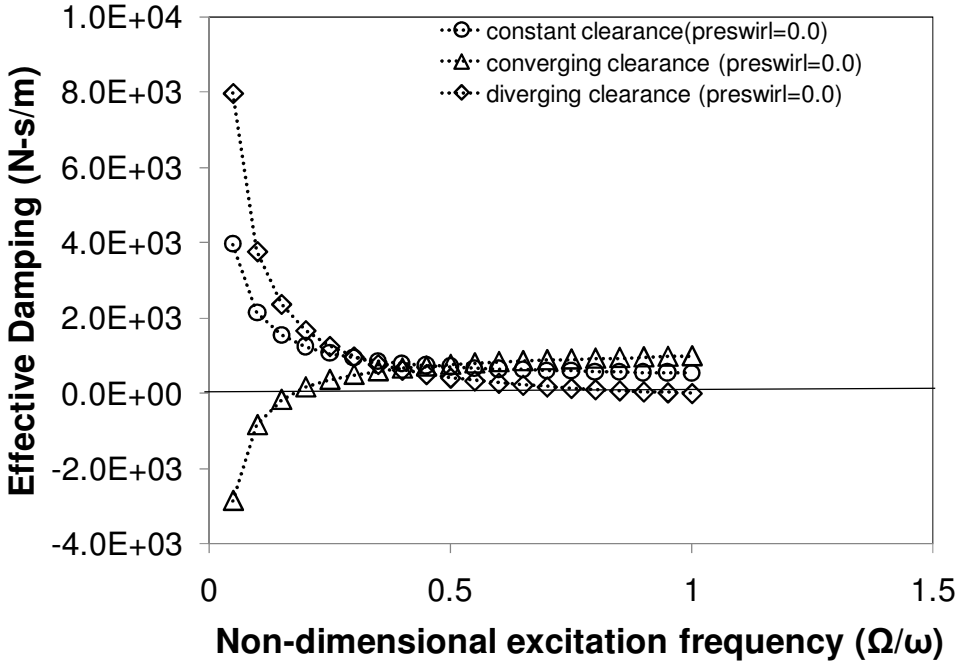

Figure 24 Effective damping versus non-dimensional excitation frequency for preswirl=0.0

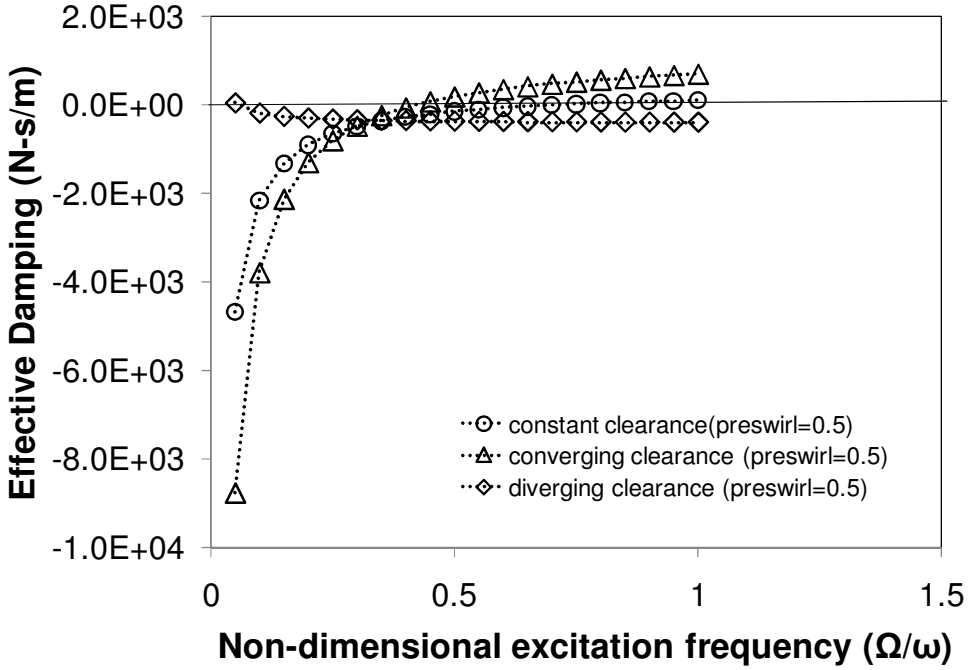

Figure 25 Effective damping versus non-dimensional excitation frequency for preswirl=0.5

The predictions based on the present test case indicates that diverging seal clearance is more destabilizing when compared with constant clearance and converging clearance seals, if the ratio of rotordynamic system natural frequency (excitation frequency) to rotor speed is greater than 0.3. The predictions also qualitatively conform to experimental results by Wright [16] and Kurohashi, et al. [5] which indicate that diverging clearance seals are more destabilizing as compared to constant clearance and converging clearance seals.

CHAPTER V

1CV ADIABATIC BULK FLOW MODEL

INTRODUCTION

Bulk flow models to date have considered the flow process in a labyrinth seal to be isothermal. Brownell et al. [39] describe an "ideal" flow in a labyrinth seal to be consisting of: isentropic throttling, no kinetic energy carryover, adiabatic flow and the gas properties to be perfect. Thus, for an "ideal" flow in a labyrinth seal, the overall process is isenthalpic. For a perfect gas, this implies that the flow is isothermal. However, factors such as kinetic energy carryover reduce the amount of energy required for throttling from tooth- to-tooth. This would imply a drop in temperature across the seal. The rotor which drags the fluid inside the seal imparts energy to the fluid, increasing its enthalpy which in turn indicates a rise in temperature. Moreover for a real gas, enthalpy is a function of pressure and temperature. Thus, an isenthalpic process does not necessarily indicate an isothermal process.

Wang et al. [40] developed a 1CV model based on model by Childs & Scharrer for labyrinth seals with steam as sealing fluid. The model evaluates axial leakage based on energy conservation with steam properties obtained through IAPWS-IF97 code [41]. Although this model evaluates axial temperature variation based on steady state energy equation, the evaluation of rotordynamic coefficients is based on isothermal model. In the present section, a comprehensive 1CV model which incorporates energy equation is developed. The energy equation is employed to evaluate both steady state variables as well as rotordynamic coefficients. Hydrocarbons which are primary working fluids in Oil & Gas applications and refrigeration services are expected to show significant deviation from ideal gas behavior. To account for this deviation, thermo-physical properties of gaseous mixtures are evaluated using a code by Huber [42] (NIST SUPERTRAPP) and incorporated in the model. An alternate adiabatic model with

working fluid governed by ideal gas properties is also developed.

Assumptions

The following assumptions are used in the derivation of governing equations:

- The flow process across the labyrinth seal is assumed to be adiabatic
- The working fluid is in a single phase
- The rotor perturbations employed to evaluate seal forces are small compared to the seal clearance
- Shear stress contribution from axial velocity component is neglected
- Temperature or enthalpy change due to KE carryover is neglected in the energy equation

GOVERNING EQUATIONS

Continuity equation

Continuity equation for a general control volume is given by [43]:

$$0 = \frac{\partial}{\partial t}\int_{C\forall} \rho d\forall + \int_{CS} \rho \vec{V} \cdot d\vec{A}$$

Applied to the cavity control volume, the continuity equation takes the form:

$$\frac{\partial}{\partial \theta}\left(\frac{\rho_i A_i V_i}{R_s}\right) + \frac{\partial}{\partial t}(\rho_i A_i) + \dot{m}_{i+1} - \dot{m}_i = 0 \tag{20}$$

Circumferential momentum equation

Momentum equation for a general control volume is given by [43]:

$$\sum F_\theta = \frac{\partial}{\partial t}\int_{C\forall} V_i \rho_i d\forall + \int_{CS} V_i \rho_i (\vec{V_i} \cdot \vec{n}) dA$$

Applied to the cavity control volume in the circumferential direction, the momentum equation takes the form:

$$-\frac{A_i}{R_s}\frac{\partial P_i}{\partial \theta}+(\tau_{ri}a_{ri}-\tau_{si}a_{si})L_i=\frac{\partial}{\partial \theta}\left(\frac{\rho_i A_i V_i^2}{R_s}\right)+\frac{\partial}{\partial t}(\rho_i A_i V_i)+\dot{m}_{i+1}V_i-\dot{m}_i V_{i-1} \quad (21)$$

where a_r and a_s are dimensionless lengths upon which shear stress acts.

Energy equation

Energy equation for a control volume is given by [43]:

$$\dot{Q}-\dot{W}=\frac{\partial}{\partial t}\int_{C\forall} e\rho d\forall+\int_{CS}\left(e+\frac{P}{\rho}\right)\rho(\vec{V}\cdot\vec{n})dA$$

In the present analysis, the flow process is assumed to be adiabatic, $\dot{Q}=0$

Power input to the fluid in the CV, $\dot{W}=$ Power loss due to rotor friction

Applied to the control volume, the energy equation takes the form:

$$\frac{\partial}{\partial t}(e_i\rho_i A_i)+\frac{\partial}{\partial \theta}\left[\left(e_i+\frac{P_i}{\rho_i}\right)\left(\frac{\rho_i V_i A_i}{R_s}\right)\right]+\dot{m}_{i+1}\left(e_{out}+\frac{P_i}{\rho_i}\right)-\dot{m}_i\left(e_{in}+\frac{P_{i-1}}{\rho_{i-1}}\right)=\tau_{ri}R_s L_i\omega \quad (22)$$

where, e_i = energy of fluid in i^{th} cavity= $\hat{u}_i$ (internal energy) + $\frac{V_i^2}{2}$ (kinetic energy of fluid)

e_{in} = energy of fluid just outside the inlet orifice of i^{th} cavity

= $\hat{u}_{i-1}$ (internal energy of fluid in $(i-1)^{th}$ cavity) + $\frac{V_{i-1}^2}{2}$ (kinetic energy of fluid in previous cavity)

As enthalpy (h) of a fluid is the sum of internal energy and flow work,

$$e_{in}+\frac{P_{i-1}}{\rho_{i-1}}=h_{i-1}+\frac{V_{i-1}^2}{2}$$

Similarly,

$$e_{out}+\frac{P_i}{\rho_i}=h_i+\frac{V_i^2}{2}$$

The energy equation can be expressed as:

$$\frac{\partial}{\partial t}\left(\left(\hat{u}_i+\frac{V_i^2}{2}\right)\rho_i A_i\right)+\frac{\partial}{\partial \theta}\left(\left(h_i+\frac{V_i^2}{2}\right)\frac{\rho_i V_i A_i}{R_s}\right)+\dot{m}_{i+1}\left(h_i+\frac{V_i^2}{2}\right)-\dot{m}_i\left(h_{i-1}+\frac{V_{i-1}^2}{2}\right) \quad (23)$$
$$=\tau_{ri} R_s L_i \omega$$

Leakage equation

Ideal throttling across a labyrinth seal tooth can be considered to be isentropic. Figure 26 shows a representation of the isentropic throttling process. St. Venant leakage equation [25] is derived using this assumption. In the present analysis, leakage is determined from isentropic throttling process across a seal tooth. After throttling, the gas undergoes isobaric expansion.

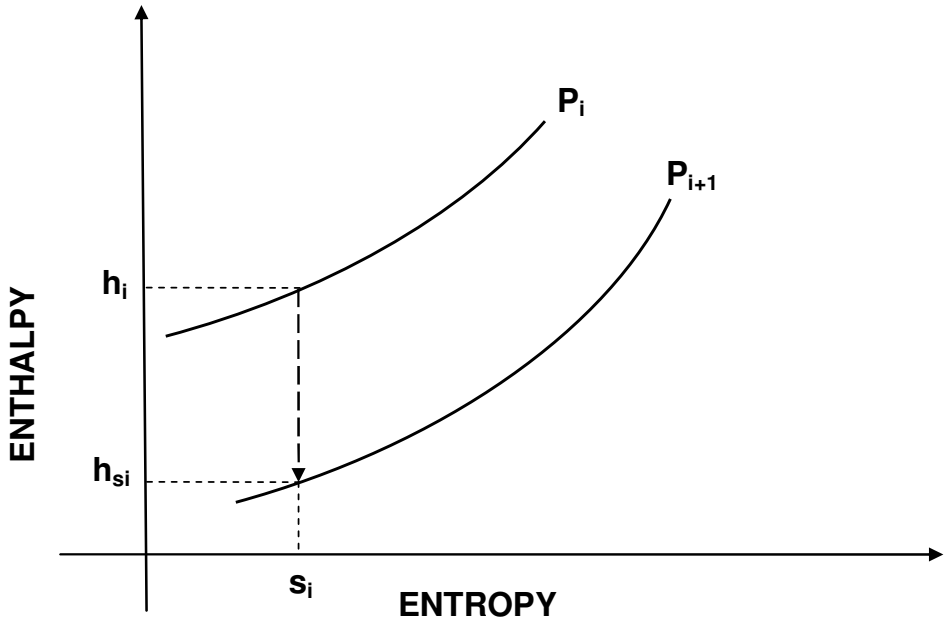

Figure 26 Plot indicating isentropic throttling on Enthalpy-Entropy (h-s) diagram

In an ideal labyrinth seal with zero rotor speed, enthalpy of the sealing fluid would be conserved assuming that there is no exchange of heat between the sealing fluid

and surroundings. However, if there is a residual kinetic energy within the seal cavity, enthalpy will not be conserved. A gradual drop in enthalpy along the length of the seal is expected with this assumption.

The axial leakage rate is determined by energy balance between the seal cavity and the constriction under the seal tooth.

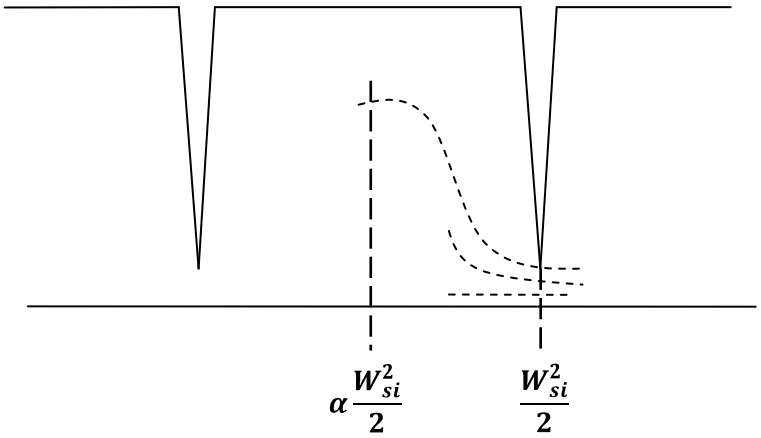

Figure 27 kinetic energy carryover (Vermes'[24])

Figure 27 shows the kinetic energy carryover effect as suggested by Vermes'[24]. The energy balance is stated as:

$$h_i + \frac{\alpha W_{si}^2}{2} = h_{si} + \frac{W_{si}^2}{2}$$

where, W_{si} and h_{si} are the axial velocity of flow and enthalpy under the seal tooth. In the present model, α is based on modified Hodkinson's [25] carryover coefficient and is given by

$$\alpha_i = \left(\frac{i-1}{i}\right)\cdot\left(\frac{C_{ri}/L_i}{(C_{ri}/L_i)+0.02}\right)$$

where, i is the tooth number.

As the thermodynamic process 1-2 is isentropic,

$$S_i = S_{si}$$

Here, S_i represents entropy in i^{th} cavity and S_{si} is the entropy under seal tooth.

If the pressure in the next cavity P_{i+1}, is known, h_{si} can be determined from thermodynamic relation between this pressure and entropy, S_i:

$$h_{si} = f(P_{i+1}, S_{si})$$

Axial velocity within the seal constriction can be estimated from Eq.(24).

$$W_{si} = \frac{1}{\sqrt{1-\alpha}}\sqrt{2(h_i - h_{si})} \tag{24}$$

The ratio, $\frac{1}{\sqrt{1-\alpha_i}}$ is the kinetic energy carryover factor

The mass flow rate can be obtained from,

$$\dot{m}_{i+1} = \rho_{si} C_{ri} c_f W_{si} \tag{25}$$

Here ρ_{si} is the density at the seal constriction and is determined from the known Pressure P_{i+1} and Entropy S_i. c_f is the flow coefficient and is assumed to be a constant 0.716 based on results by Eser & Kazakia [36].

Thus, the leakage calculated under a tooth is a function of pressure and enthalpy in the previous cavity and pressure in the next cavity

$$m_i = \phi(P_{i-1}, h_{i-1}, P_i) \tag{26}$$

For the gas with ideal gas properties, the above leakage equation reduces to the form as shown in Eq.27. This leakage equation is one of the leakage models recommended by Gamal [25]:

$$\dot{m}_i = \frac{1}{\sqrt{1-\alpha_i}} \frac{c_f C_{ri} P_{i-1}}{\sqrt{\gamma R T_{i-1}}} \sqrt{\frac{2\gamma^2}{\gamma - 1}\left(\left(\frac{P_i}{P_{i-1}}\right)^{\frac{2}{\gamma}} - \left(\frac{P_i}{P_{i-1}}\right)^{\frac{\gamma+1}{\gamma}}\right)} \tag{27}$$

Zeroth order equations

Continuity equation

The zeroth-order continuity equation reduces to:

$$\dot{m}_i = \dot{m}_{i+1} = \dot{m}_0 \tag{28}$$

Equation (26) provides definition for $\dot{m}_i$.

Circumferential momentum equation

$$\dot{m}_0(V_i - V_{i-1}) = (\tau_{ri} a_{ri} - \tau_{si} a_{si}) L_i \tag{29}$$

Energy equation

$$\dot{m}_0\left(h_i + \frac{V_i^2}{2} - h_{i-1} - \frac{V_{i-1}^2}{2}\right) = \tau_{ri} R_s L_i \omega \tag{30}$$

Solution procedure

For an assumed leakage rate, the pressure in the first cavity is determined by solving the leakage equation. The enthalpy and velocity in the first cavity is determined by solving the coupled circumferential momentum equation and the energy equation. Multi-variate Newton Raphson iteration procedure is employed to obtain the solution for velocity and enthalpy. This procedure is repeated for cavities downstream until the exit pressure is estimated. If the calculated exit pressure is less than the actual exit pressure, the assumed mass flow rate is decreased and vice-versa. Thus, a bisection method root solving algorithm is used to estimate the mass flow rate.

To ensure adequate scaling of terms in the governing equations, the variables are non-dimensionalized as follows:

$$
\begin{aligned}
p_i &= \frac{P_i}{P_R} & \tau &= t\omega & \tilde{u}_e &= \frac{\hat{u}_R}{(R_s\omega)^2} \\
\tilde{\rho}_i &= \frac{\rho_i}{\rho_R} & \tilde{u}_i &= \frac{\hat{u}_i}{\hat{u}_R} & \tilde{h}_e &= \frac{h_R}{(R_s\omega)^2} \\
v_i &= \frac{V_i}{R_s\omega} & a_i &= \frac{A_i}{A_{0i}} & \lambda_s &= \frac{a_{si}L_iR_s}{A_{0i}} \\
\xi_i &= \frac{H_i}{C_{ri}} & \tilde{h}_i &= \frac{h_i}{h_R} & \lambda_r &= \frac{a_{ri}L_iR_s}{A_{0i}} \\
l_i &= \frac{L_i}{R_s} & \sigma_i &= \frac{\rho_R A_{0i}\omega}{\dot{m}_0} & \tilde{\tau}_{ri} &= \frac{\tau_{ri}}{\rho_R(R_s\omega)^2} \\
b_i &= \frac{B_i}{L_i} & P_e &= \frac{P_R}{\rho_R(R_s\omega)^2} & \tilde{\tau}_{si} &= \frac{\tau_{si}}{\rho_R(R_s\omega)^2} \\
 & & f &= \frac{\Omega}{\omega} & \tilde{\dot{m}}_i &= \frac{\dot{m}_i}{\dot{m}_0}
\end{aligned}
\tag{31}
$$

Internal energy, density and viscosity are obtained via NIST SUPERTRAPP code. For the model with ideal gas properties, following relations for internal energy, enthalpy, density and viscosity are used:

$$
\begin{aligned}
\hat{u}_i &= C_v T_i \\
\hat{h}_i &= C_p T_i \\
\rho_i &= \frac{P_i}{RT_i}
\end{aligned}
\tag{32}
$$

Viscosity is assumed to vary according to power law [43] with temperature

$$
\mu_i = \mu_0 \left(\frac{T_i}{T_0} \right)^{0.7} \tag{33}
$$

Non-dimensionalized Governing Equations are:

Continuity equation

$$
\tilde{\sigma}_i \left\{ \frac{\partial}{\partial \tau}\left(\tilde{\rho}_i a_i\right) + \frac{\partial}{\partial \theta}\left(\tilde{\rho}_i a_i v_i\right) \right\} + \dot{\tilde{m}}_{i+1} - \dot{\tilde{m}}_i = 0 \tag{34}
$$

Circumferential momentum equation

$$\tilde{\sigma}_i\left\{\frac{\partial}{\partial\tau}\left(\tilde{\rho}_i a_i v_i\right)+\frac{\partial}{\partial\theta}\left(\tilde{\rho}_i a_i v_i^2\right)\right\}+\tilde{\sigma}_i P_e a_i\frac{\partial p_i}{\partial\theta}+\tilde{\sigma}_i\left\{\lambda_s\tilde{\tau}_{si}-\lambda_r\tilde{\tau}_{ri}\right\}+\dot{\tilde{m}}_{i+1}v_i-\dot{\tilde{m}}_i v_{i-1}=0 \qquad (35)$$

Energy equation

$$\begin{aligned}&\tilde{\sigma}_i\left\{\frac{\partial}{\partial\tau}\left(\left(\tilde{u}_i\tilde{u}_e+\frac{v_i^2}{2}\right)\tilde{\rho}_i a_i\right)+\frac{\partial}{\partial\theta}\left(\left(\tilde{h}_i\tilde{h}_e+\frac{v_i^2}{2}\right)\tilde{\rho}_i a_i v_i\right)\right\}+\dot{\tilde{m}}_{i+1}\left(\tilde{h}_i\tilde{h}_e+\frac{v_i^2}{2}\right)\\&-\dot{\tilde{m}}_i\left(\tilde{h}_{i-1}\tilde{h}_e+\frac{v_{i-1}^2}{2}\right)=\tilde{\sigma}_i\lambda_r\tilde{\tau}_{ri}\end{aligned} \qquad (36)$$

To solve for the rotordynamic coefficients, perturbation analysis is employed. Eccentricity ratio $\boldsymbol{\varepsilon}$ is used as the perturbation parameter. First order solution of the governing equations determines the pressure and velocity perturbations due rotor perturbation.

$$\begin{aligned}\tilde{h}_i&=\tilde{h}_{0i}+\varepsilon\tilde{h}_{1i}\\v_i&=v_{0i}+\varepsilon v_{1i}\\p_i&=p_{0i}+\varepsilon p_{1i}\\\tilde{\rho}_i&=\tilde{\rho}_{0i}+\varepsilon\tilde{\rho}_{1i}\\a_i&=a_{0i}+\varepsilon a_{1i}\\\xi&=\xi_0+\varepsilon\eta=\xi_0-x\cos\theta-y\sin\theta\end{aligned} \qquad (37)$$

First order equations

Equations (38-40) represent the first order governing equations and define the pressure, circumferential velocity and temperature fluctuations due to rotor perturbation.

Continuity equation

$$\begin{aligned}&\tilde{\sigma}_{0i}\{\frac{\partial\tilde{\rho}_{0i}}{\partial p_{0i}}\frac{\partial p_{1i}}{\partial\tau}+\frac{\partial\tilde{\rho}_{0i}}{\partial\tilde{h}_{0i}}\frac{\partial\tilde{h}_{1i}}{\partial\tau}+\tilde{\rho}_{0i}\beta_{0i}\frac{\partial\eta}{\partial\tau}+v_{0i}\frac{\partial\tilde{\rho}_{0i}}{\partial p_{0i}}\frac{\partial p_{1i}}{\partial\theta}+v_{0i}\frac{\partial\tilde{\rho}_{0i}}{\partial\tilde{h}_{0i}}\frac{\partial\tilde{h}_{1i}}{\partial\theta}\\&+\tilde{\rho}_{0i}\frac{\partial v_{1i}}{\partial\theta}+\tilde{\rho}_{0i}v_{0i}\beta_{0i}\frac{\partial\eta}{\partial\theta}\}+\frac{\partial\dot{\tilde{m}}_{0i+1}}{\partial p_{0i+1}}p_{1i+1}+\frac{\partial\dot{\tilde{m}}_{0i+1}}{\partial p_{0i}}p_{1i}-\frac{\partial\dot{\tilde{m}}_{0i}}{\partial p_{0i}}p_{1i+1}\\&-\frac{\partial\dot{\tilde{m}}_{0i}}{\partial p_{0i-1}}p_{1i-1}=0\end{aligned}\tag{38}$$

Circumferential momentum equation

$$\begin{aligned}&\tilde{\sigma}_{0i}\{v_{0i}\frac{\partial\tilde{\rho}_{0i}}{\partial p_{0i}}\frac{\partial p_{1i}}{\partial\tau}+v_{0i}\frac{\partial\tilde{\rho}_{0i}}{\partial\tilde{h}_{0i}}\frac{\partial\tilde{h}_{1i}}{\partial\tau}+\tilde{\rho}_{0i}v_{0i}\beta_{0i}\frac{\partial\eta}{\partial\tau}+\tilde{\rho}_{0i}\frac{\partial v_{1i}}{\partial\tau}+v_{0i}^2\frac{\partial\tilde{\rho}_{0i}}{\partial p_{0i}}\frac{\partial p_{1i}}{\partial\theta}\\&+v_{0i}^2\frac{\partial\tilde{\rho}_{0i}}{\partial\tilde{h}_{0i}}\frac{\partial\tilde{h}_{1i}}{\partial\theta}+2\tilde{\rho}_{0i}v_{0i}\frac{\partial v_{1i}}{\partial\theta}+\tilde{\rho}_{0i}v_{0i}^2\beta_{0i}\frac{\partial\eta}{\partial\theta}\}+\tilde{\sigma}_{0i}P_e\frac{\partial p_{1i}}{\partial\theta}+\tilde{\sigma}_{0i}\{\lambda_s\tilde{\tau}_{1si}-\lambda_r\tilde{\tau}_{1ri}\}\\&+v_{0i}\frac{\partial\dot{\tilde{m}}_{0i+1}}{\partial p_{0i+1}}p_{1i+1}+v_{0i}\frac{\partial\dot{\tilde{m}}_{0i+1}}{\partial p_{0i}}p_{1i}-v_{0i-1}\frac{\partial\dot{\tilde{m}}_{0i}}{\partial p_{0i}}p_{1i+1}-v_{0i-1}\frac{\partial\dot{\tilde{m}}_{0i}}{\partial p_{0i-1}}p_{1i-1}+\dot{\tilde{m}}_0v_{1i}\\&-\dot{\tilde{m}}_0v_{1i-1}=0\end{aligned}\tag{39}$$

Energy equation

$$\begin{aligned}&\tilde{\sigma}_{0i}\{\tilde{\rho}_{0i}\tilde{u}_e\frac{\partial\tilde{u}_{0i}}{\partial p_{0i}}\frac{\partial p_{1i}}{\partial\tau}+\tilde{\rho}_{0i}\tilde{u}_e\frac{\partial\tilde{u}_{0i}}{\partial\tilde{h}_{0i}}\frac{\partial\tilde{h}_{1i}}{\partial\tau}+\tilde{u}_{0i}\tilde{u}_e\frac{\partial\tilde{\rho}_{0i}}{\partial p_{0i}}\frac{\partial p_{1i}}{\partial\tau}+\tilde{u}_{0i}\tilde{u}_e\frac{\partial\tilde{\rho}_{0i}}{\partial\tilde{h}_{0i}}\frac{\partial\tilde{h}_{1i}}{\partial\tau}+\tilde{u}_{0i}\tilde{u}_e\tilde{\rho}_{0i}\beta_{0i}\frac{\partial\eta}{\partial\tau}\\&+\frac{v_{0i}^2}{2}\frac{\partial\tilde{\rho}_{0i}}{\partial p_{0i}}\frac{\partial p_{1i}}{\partial\tau}+\frac{v_{0i}^2}{2}\frac{\partial\tilde{\rho}_{0i}}{\partial h_{0i}}\frac{\partial h_{1i}}{\partial\tau}+\tilde{\rho}_{0i}v_{0i}\frac{\partial v_{1i}}{\partial\tau}+\frac{v_{0i}^2}{2}\tilde{\rho}_{0i}\beta_{0i}\frac{\partial\eta}{\partial\tau}\}\\&\tilde{\sigma}_{0i}\{\tilde{\rho}_{0i}v_{0i}\tilde{h}_e\frac{\partial\tilde{h}_{1i}}{\partial\theta}+\tilde{\rho}_{0i}\tilde{h}_{0i}\tilde{h}_e\frac{\partial v_{1i}}{\partial\theta}+v_{0i}\tilde{h}_{0i}\tilde{h}_e\frac{\partial\tilde{\rho}_{0i}}{\partial p_{0i}}\frac{\partial p_{1i}}{\partial\theta}+v_{0i}\tilde{h}_{0i}\tilde{h}_e\frac{\partial\tilde{\rho}_{0i}}{\partial\tilde{h}_{0i}}\frac{\partial\tilde{h}_{1i}}{\partial\theta}+v_{0i}\tilde{h}_{0i}\tilde{h}_e\tilde{\rho}_{0i}\beta_{0i}\frac{\partial\eta}{\partial\theta}\\&+\frac{\tilde{\rho}_{0i}v_{0i}^3}{2}\beta_{0i}\frac{\partial\eta}{\partial\theta}+\frac{3\tilde{\rho}_{0i}v_{0i}^2}{2}\frac{\partial v_{1i}}{\partial\theta}+\frac{v_{0i}^3}{2}\frac{\partial\tilde{\rho}_{0i}}{\partial\tilde{h}_{0i}}\frac{\partial\tilde{h}_{1i}}{\partial\theta}+\frac{v_{0i}^3}{2}\frac{\partial\tilde{\rho}_{0i}}{\partial p_{0i}}\frac{\partial p_{1i}}{\partial\theta}\}\\&+\left(\tilde{h}_e\tilde{h}_{0i}+\frac{v_{0i}^2}{2}\right)\left(\frac{\partial\dot{\tilde{m}}_{0i+1}}{\partial p_{0i+1}}p_{1i+1}+\frac{\partial\dot{\tilde{m}}_{0i+1}}{\partial p_{0i}}p_{1i}\right)-\left(\tilde{h}_e\tilde{h}_{0i-1}+\frac{v_{0i-1}^2}{2}\right)\left(\frac{\partial\dot{\tilde{m}}_{0i}}{\partial p_{0i}}p_{1i+1}+\frac{\partial\dot{\tilde{m}}_{0i}}{\partial p_{0i-1}}p_{1i-1}\right)\\&+\dot{\tilde{m}}_0\left(\tilde{h}_e\tilde{h}_{1i}+v_{0i}v_{1i}-\tilde{h}_e\tilde{h}_{1i-1}-v_{0i-1}v_{1i-1}\right)=\tilde{\sigma}_{0i}\lambda_r\tilde{\tau}_{1ri}\end{aligned}\tag{40}$$

Separation of variables approach is used to solve the partial differential equations:

$$\begin{aligned} \varepsilon\eta &= -r_0 e^{j(f\tau-\theta)} \\ p_{1i} &= \hat{p}_{1i} e^{j(f\tau-\theta)} \\ v_{1i} &= \hat{v}_{1i} e^{j(f\tau-\theta)} \\ \tilde{h}_{1i} &= \hat{\tilde{h}}_{1i} e^{j(f\tau-\theta)} \end{aligned} \tag{41}$$

The separation of variables approach leads to the following system of equations

$$[A]_{3\times3}\{x\}_{i-1} + [B]_{3\times3}\{x\}_i + [C]_{3\times3}\{x\}_{i+1} = \frac{r_0}{\varepsilon}\{D_{3\times1}\}_i \tag{42}$$

The matrix coefficients and the procedure to determine radial and circumferential dynamic stiffness coefficient are elaborated in Appendix B.

COMPARISON OF ZEROTH ORDER PREDICTIONS WITH EXPERIMENTAL RESULTS

Validation of a model relies on the conformity to experimental results. The zeroth order solution can be verified by comparison with experimental temperature distribution in a labyrinth seal. The current interest in the thermal effects of labyrinth seal flow is in improving the efficiency of gas turbine/compressors through minimizing secondary losses. The viscous drag on the rotating components represent power loss as well heat input to cooling air system of a gas turbine engine. Several experimental investigations are available in the literature to measure the windage loss due a labyrinth seal. McGreehan and Ko [26] provide experimental results for temperature rise across a stepped seal. The authors also present analytical correlation to obtain the temperature distribution in a seal. Millwards and Edwards [27] consider the effect of leakage flow on temperature rise in labyrinth seals. Experimental investigations by Denecke et al. [28] consider the effect of inlet swirl on windage loss.

The 1CV model with energy equation is employed to predict the experimental results by Denecke et al. [28]. Note that the authors tested a stepped labyrinth seal.

Accordingly the governing equations are modified to account for the geometry of the stepped seal. The zeroth order continuity and circumferential momentum equations are similar to those derived by Scharrer [44] for a stepped labyrinth. For a stepped seal, the kinetic energy carryover factor is insignificant and hence neglected in the analysis.

The predictions are also compared with CFD results by Denecke et al. [28]. Table 10 provides the seal dimensions considered in the analysis. Convergent and divergent stepped labyrinth seals are considered in the analysis.

Table 10: Seal Parameters (all dimensions in mm)

Inlet Radius	256 /250
Exit Radius	250 /256
Tooth height	4
Tooth pitch	8
Clearance	1.3
Tip width	0.4
Step height	2
Number of Teeth	4

The operating conditions and test results are represented in the form of dimensionless numbers. The dimensionless numbers of interest are:

- Windage heating number,σ

$$\sigma = \frac{2C_p \Delta T_{tot}}{U^2} \tag{43}$$

  where U is the average rotor circumferential velocity, $U=R_s\,\omega$.

  The windage heating number is indicative of the windage loss and the temperature rise of the sealing fluid.

- Axial Reynolds number, Re

$$\mathrm{Re} = \frac{\dot{m}_0}{\mu \pi R_s}$$

- Circumferential Mach number, M_U

$$M_U = \frac{U}{c_0}$$

where, c_0 = speed of sound at entrance

$$c_0 = \sqrt{\gamma R T_{in}}$$

- Effective pressure ratio, Π

$$\Pi = \frac{P_{in}}{P_{out}} \left(1 + \frac{\gamma - 1}{\gamma} K_{in}^2 M_U^2 \right)^{-\frac{\gamma}{\gamma - 1}} \tag{44}$$

where, K_{in} is the inlet swirl to the labyrinth.

The effective pressure ratio considers the effect of fluid preswirl on leakage.

Table 11 provides the operating conditions considered in the analysis.

Table 11: Operating conditions

Re	10000, 20000
Π	1.05, 1.3
P_{in}	2 bar
T_{in}	300 K

Figure 28 (a) shows the variation of windage loss factor with circumferential Mach number at axial flow Reynolds number, Re of 10000 for converging flow. Note that Re = 10000, is obtained for effective pressure ratio of 1.05 experimentally and 1.058 in the analytical prediction. The plot indicates that the 1CV model over-predicts the temperature rise as compared to the experimental values, whereas the CFD predictions by the authors under-predict the windage loss. Figure 28 (b) indicates that 1CV predictions closely match the experimental and CFD predictions for axial flow Reynolds number, Re=20000. 1CV model requires a pressure ratio of 1.23 to obtain this Reynolds

number. Comparison between Fig. 28 (a) and Fig. 28(b) indicates that as axial flow increases, the windage heating number reduces.

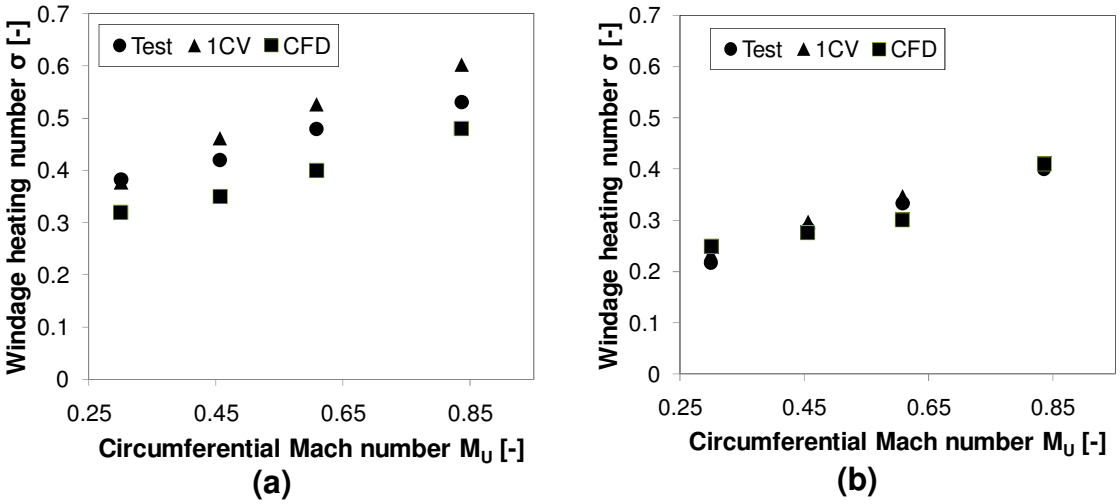

Figure 28 Windage heating number versus circumferential Mach number at (a) Re = 10000 and (b) Re = 20000, convergent flow direction

Figures 29 (a-b) indicate the influence of preswirl on the windage loss factor for divergent stepped seal. 1CV predictions closely match the experimental values at higher preswirl (preswirl=0.3). The plots also indicate that preswirl reduces the temperature rise and thus the windage loss factor. This is due to the fact that with more preswirl, the work done by the rotor in dragging the fluid to its equilibrium circumferential velocity reduces. This decrease in work done by the rotor clearly reflects in the decrease of windage power loss factor.

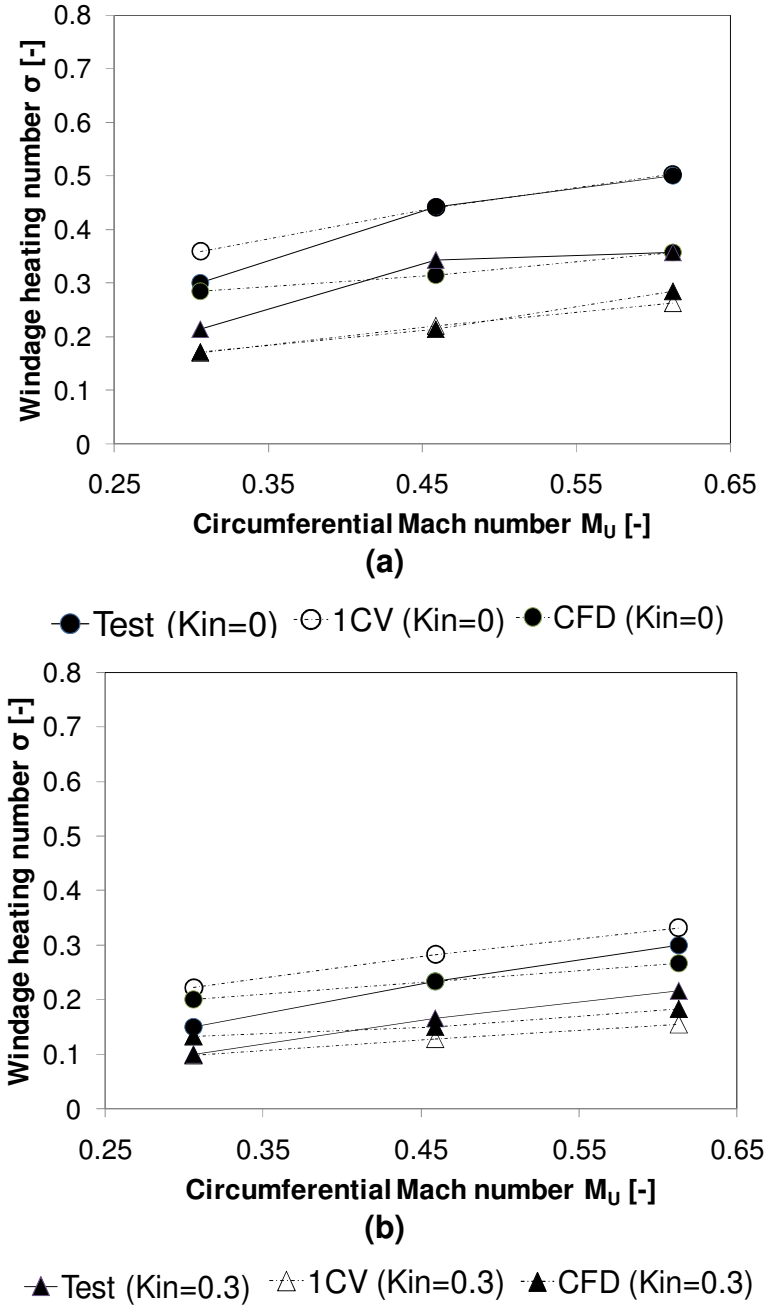

Figure 29 Windage heating number versus circumferential Mach number at (a) Re = 10000 and (b) Re = 20000, divergent flow direction

Thus, the predictions based on 1CV model with energy equation agree well with experimental results.

COMPARISON OF ROTORDYNAMIC COEFFICIENTS

Although in the previous section, the zeroth order solution is validated against experimental results, rotordynamic test data are not available for the same test case. A test case of Picardo [17] for which extensive data are available is considered for comparison. For higher axial flow, the temperature rise across the seal is expected to be minimal. Therefore, the impact of the energy equation on the predicted results is expected to be minimal.

Table 1 provides the seal geometry. Inlet pressure of 70 bar is considered. Air is the working fluid. As fluid properties of air are closer to that of an ideal gas, a minimal difference is expected between the two adiabatic models.

Table 12 provides molar composition of air which is used as input to the NIST supertrapp code to obtain thermo-physical properties.

Table 12: Molar composition of air

Nitrogen	0.78084
Oxygen	0.20951
Argon	0.00934
Carbon dioxide	0.00031

Figures (30-33) compares measured direct and cross-coupled stiffness and damping with 1CV isothermal, 1CV adiabatic (ideal gas) and 1CV adiabatic (real gas) models. The comparison is provided for three different rotor speeds 10200 rpm, 15200 rpm and 20200 rpm, and two different back pressures 36% and 52%. At lower rotor speeds, all three models show comparable results. However as rotor speeds increase, the adiabatic flow models show improved predictions as compared to the isothermal model.

Comparison of cross-coupled stiffness, direct and cross-coupled damping shows that the isothermal model performs better in predicting the measured results. In all the comparisons, the difference between adiabatic (ideal gas) and adiabatic (real gas) is minimal and can be considered negligible for practical purposes.

Comparison of experimental results shows negligible difference between the model predictions based on real gas and ideal gas properties. This is expected as the working fluid considered is air which shows close to ideal gas behavior. The models however are expected to show considerable difference for hydrocarbons which show considerable deviation from ideal gas behavior. For the experimental results by Picardo, the isothermal 1CV model shows better correlation as compared to the adiabatic flow models.

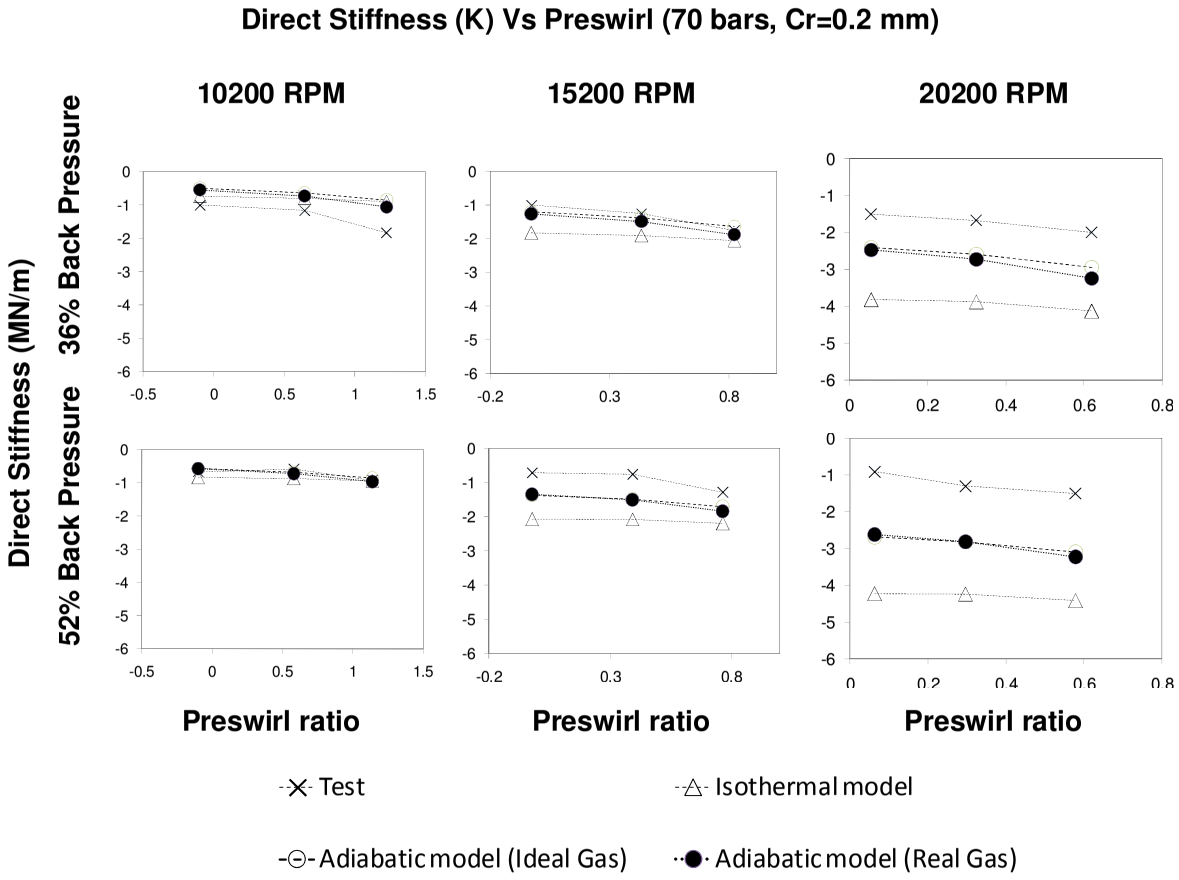

Figure 30 Predictions versus measured direct stiffness

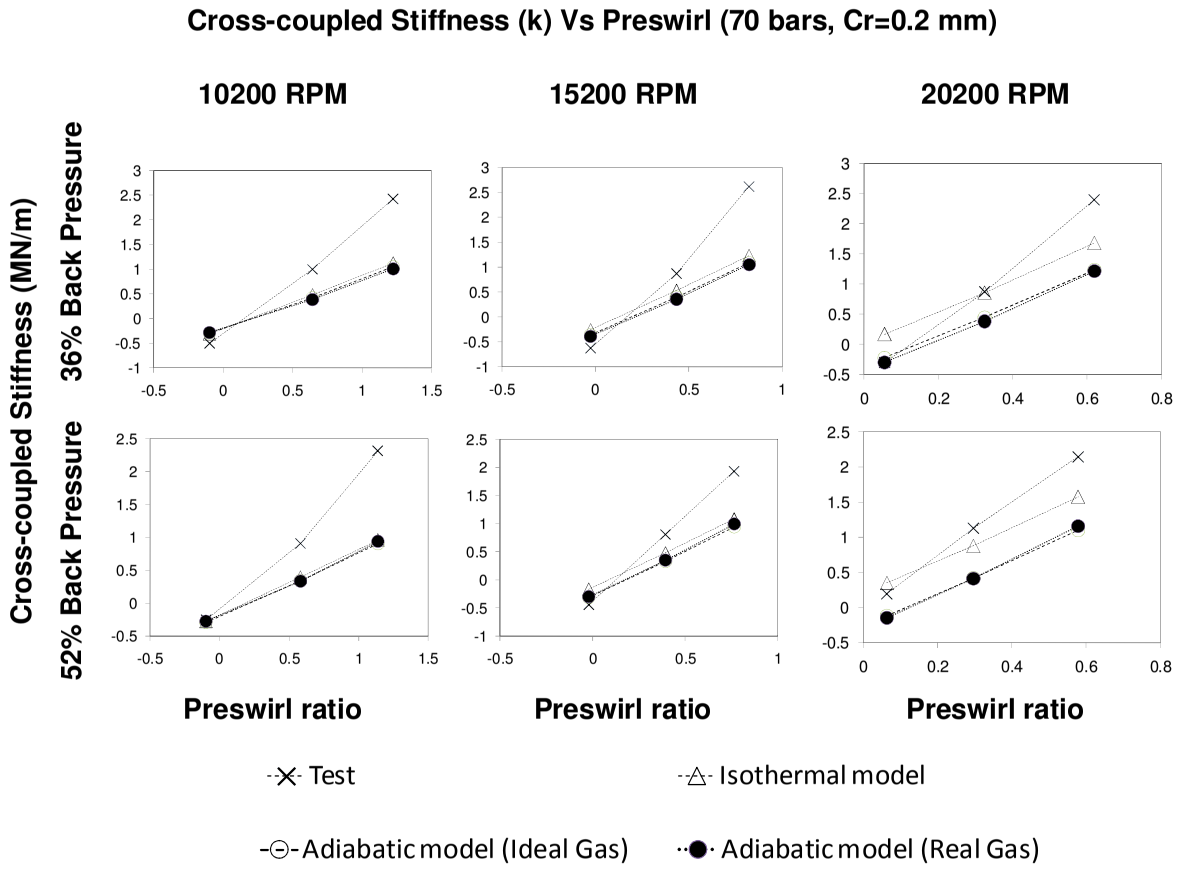

Figure 31 Predictions versus measured cross-coupled stiffness

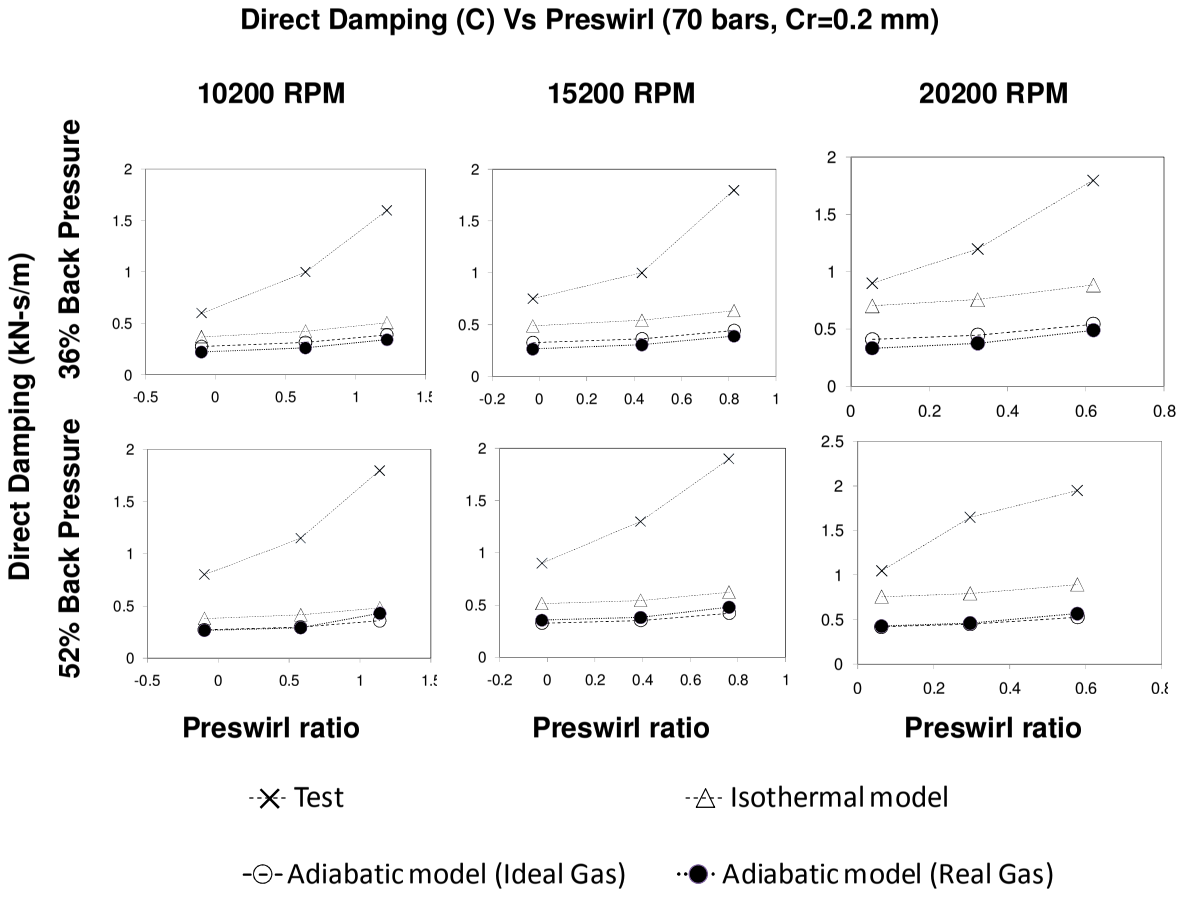

Figure 32 Predictions versus measured direct damping for Cr=0.2 mm

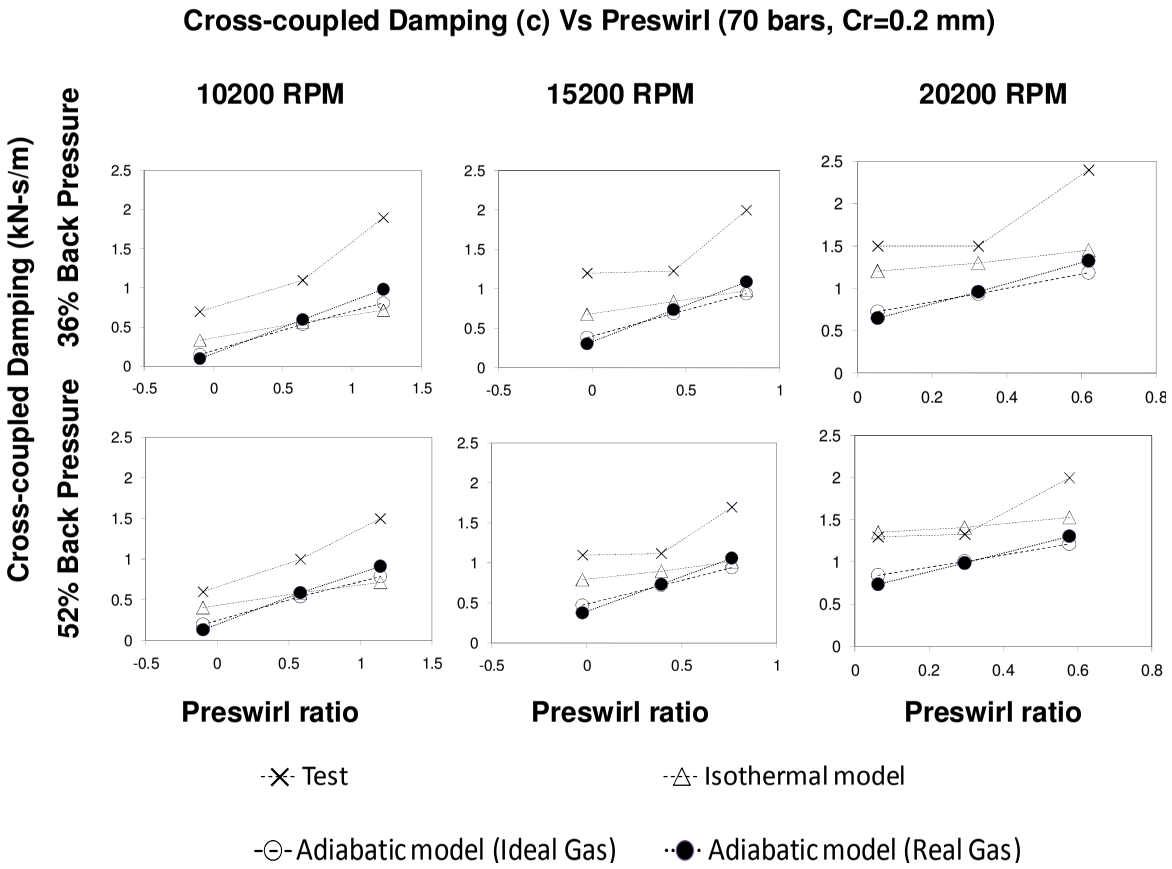

Figure 33 Predictions versus measured cross-coupled damping for Cr=0.2 mm

CHAPTER VI

IMPACT OF REAL GAS PROPERTIES ON STATIC AND ROTORDYNAMIC CHARACTERISTICS OF A GAS LABYRINTH SEAL

INTRODUCTION

The objective of the present analysis is to gauge the impact of deviation of properties of real gases from ideal gas laws on static and rotordynamic characteristics of a labyrinth seal. Shin and Childs [45] considered a test case for annular hole-patterned (HP) seal using Methane as the sealing fluid. Labyrinth seal geometry similar to their test seal is considered in the present case. Two test cases with Methane and Carbon dioxide are presented. A One control volume (1CV) model which assumes adiabatic flow conditions with the thermo-physical properties of the sealing fluid obtained from National Institute of Standards (NIST) is used to assess the effect of real gas properties on predictions. The static and dynamic characteristics are compared with 1CV adiabatic flow model with ideal gas properties and 1CV model by Childs & Scharrer [6].

Seal geometry

Table 13 provides the seal geometry for annular hole-pattern seal considered by Shin and Childs [45].

Table 13: Hole- pattern seal geometry (All dimensions in mm)

Seal diameter	250
Seal Length	150
Radial clearance	0.3
Hole depth	2

For the present analysis, a labyrinth seal with the same seal length and diameter is considered. Arbitrary tooth pitch and tooth height are assigned. The radial clearance is reduced to 0.2 mm to approximately match the flow-rate of the original seal. Table 14 provides the corresponding Labyrinth seal parameters.

Table 14: Labyrinth seal geometry (All dimensions in mm)

Seal diameter	250
Seal Length	150
Radial clearance	0.2
Tooth pitch	7.5
Tooth height	6
Number of teeth	20

METHANE GAS COMPRESSOR TEST SEAL

Shin and Childs [45] provide a test case for a high pressure methane gas compressor. Table 15 provides their operating conditions.

Table 15: Operating conditions for Methane gas compressor seal

Inlet Pressure	1034.2 bars
Exit Pressure	620.5 bars
Inlet temperature	400 K
Rotor speed	10000 rpm

Thermo-physical properties of Methane at seal inlet obtained using NIST code are provided in Table 16.

Table 16: Thermo-physical properties of Methane at inlet temperature and pressure

γ (ratio of specific heats)	1.408
C_p (Specific heat at constant pressure)	3.259 KJ/kg K
Viscosity	3.88×10^{-5} Pa-s
Inlet Density	285.6 kg/m^3
Inlet gas compressibility	1.74

The calculated mass-flow rates for the three models (Isothermal, Adiabatic Ideal gas and Adiabatic Real gas) are 6.22 kg/s, 6.21kg/s and 5.04 kg/s respectively. Real gas code computes a value of leakage rate which is significantly different than ideal gas codes as it accounts for compressibility correction factor-Z. Note that Z-factor is greater than 1 for the given operating conditions which accounts for the low leakage rate obtained using real gas properties.

The pressure and circumferential velocity distribution is very similar for the three models. Figure 34 provides temperature distribution for the three models.

The adiabatic real gas model shows a higher rise in temperature compared to the other two models. Note that Joule-Thompson coefficient is negative (-0.3858 K/MPa at seal inlet) in the operating region. As the pressure drops along the seal length, temperature rises due to this effect. The net rise in temperature is thus a combination of Joule-Thompson effect and due to the power transmitted to the sealing fluid through the rotor.

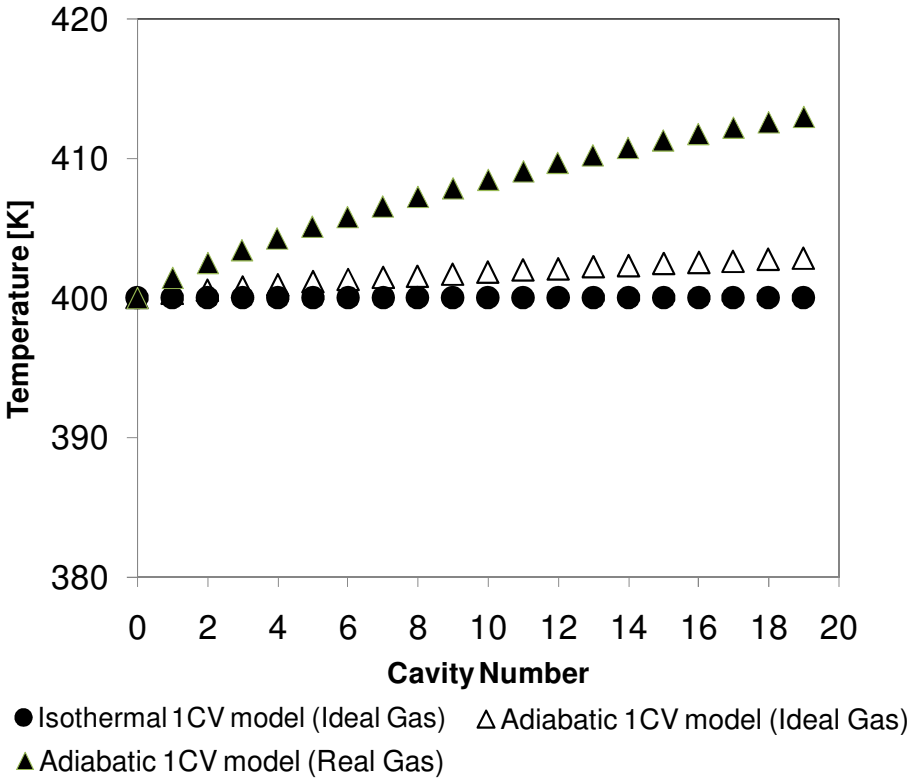

Figure 34 Temperature distribution along the seal length for Methane

Rotordynamic coefficients are evaluated for three different inlet preswirl conditions. Figure 35 shows the variation of effective damping coefficients for the three models. The plots indicate that adiabatic models yield more conservative results (lesser damping) as compared to the isothermal model. Effective damping is least for the model which incorporates real gas properties at lower preswirl ratios.

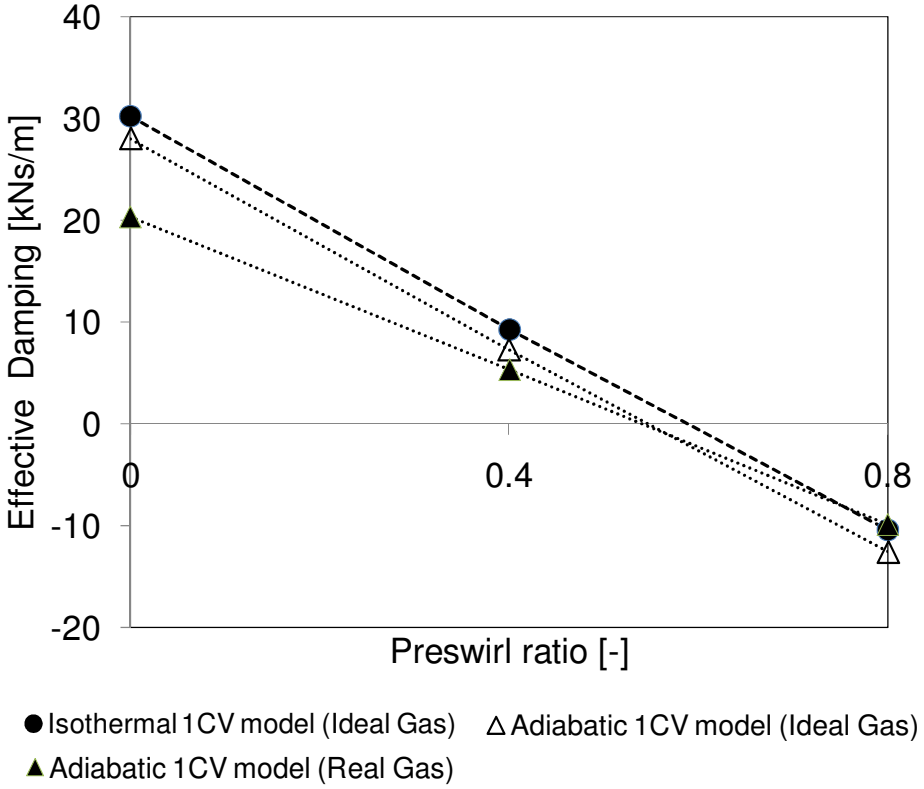

Figure 35 Effective damping versus preswirl ratio for Methane

Figure 36 depicts variation of direct stiffness with preswirl for the three models. Real gas model shows lowest negative stiffness among the three models. This discrepancy can be attributed to the predicted low leakage flow rate for the real gas model.

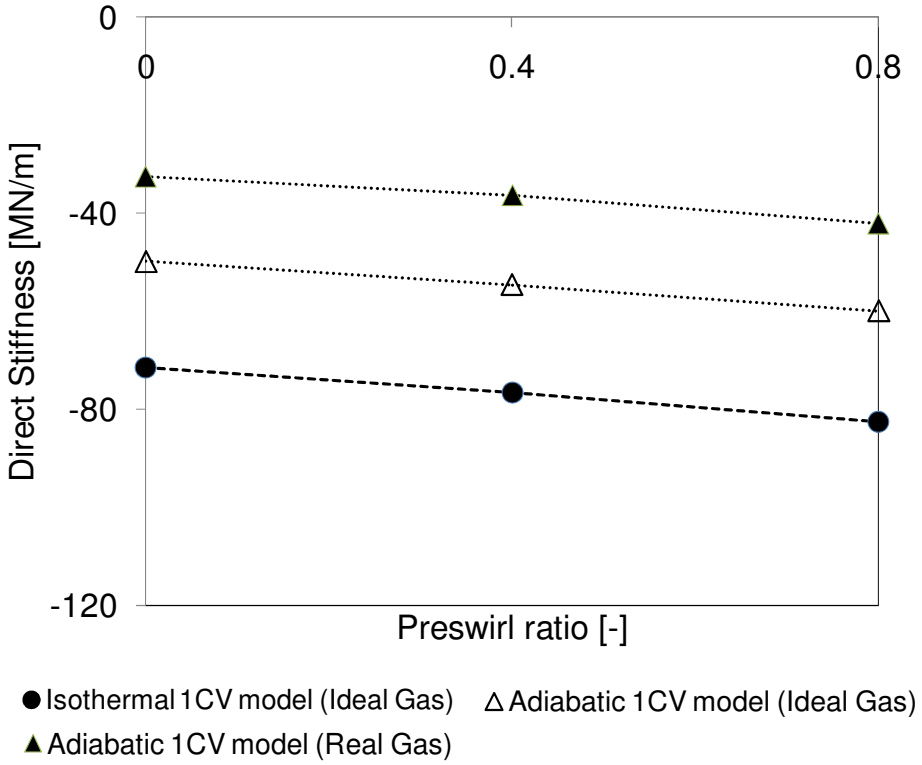

Figure 36 Direct stiffness versus preswirl ratio for Methane

TEST CASE FOR CARBON DIOXIDE

A test case for Carbon dioxide is considered in the present case where the Z-factors within the operating region are less than 1. The leakage flow rates computed using real gas properties are expected to be greater than those calculated using ideal properties for Z-factors less than one.

Table 17 lists the operating conditions with CO_2 as the sealing fluid. The seal geometry considered is the same as described in Table 14.

Table 17: Operating conditions for Carbon dioxide compressor seal

Inlet Pressure	100 bar
Exit Pressure	40 bar
Inlet temperature	350 K

Properties of CO_2 at seal inlet are obtained using NIST code and are tabulated in Table 18.

Table 18: Thermo-physical properties of Carbon dioxide at seal inlet temperature and pressure

γ (Ratio of specific heats)	2.236
C_p (Specific heat at constant pressure)	1.943 kJ/kg K
Viscosity	2.333×10^{-5} Pa-s
Inlet Density	226.1 kg/m^3
Inlet gas compressibility	0.669

Mass flow-rates evaluated for Isothermal, Adiabatic Ideal and Adiabatic Real models are 1.225 kg/s, 1.217 kg/s and 1.42 kg/s respectively. In this case, the leakage rate estimated by Real gas model is higher as compared to other models which can be attributed to the less than unity Z-factor.

The pressure and circumferential velocity distribution is almost similar for all the models. Figures 37 and 38 illustrate temperature distribution for the three models at rotor speeds of 3.6 krpm and 10 krpm respectively.

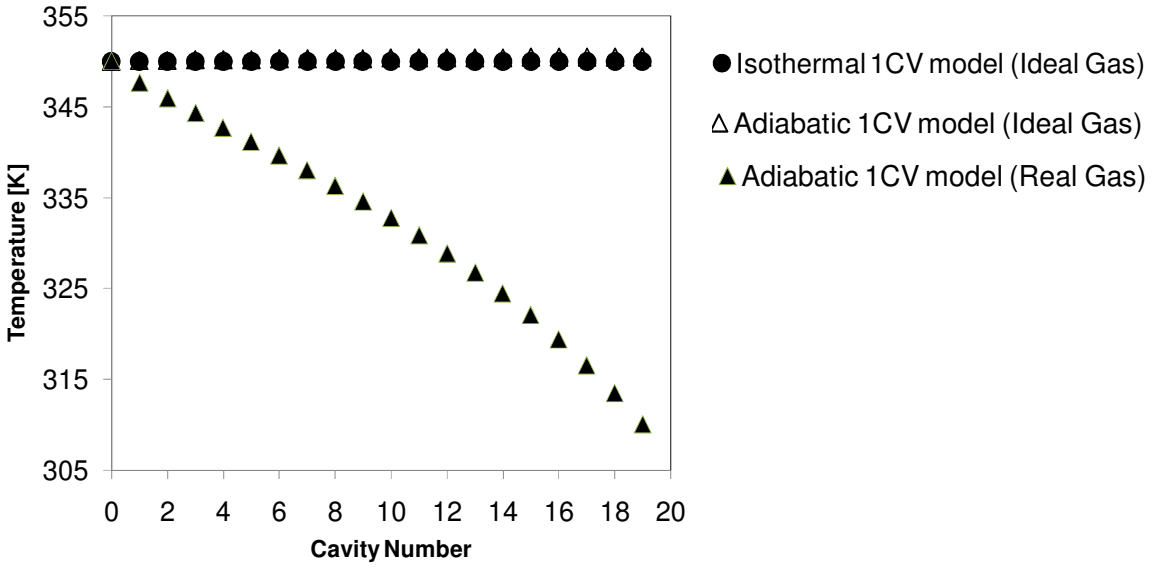

Figure 37 Temperature distribution along the seal length at rotor speed=3.6krpm for Carbon dioxide

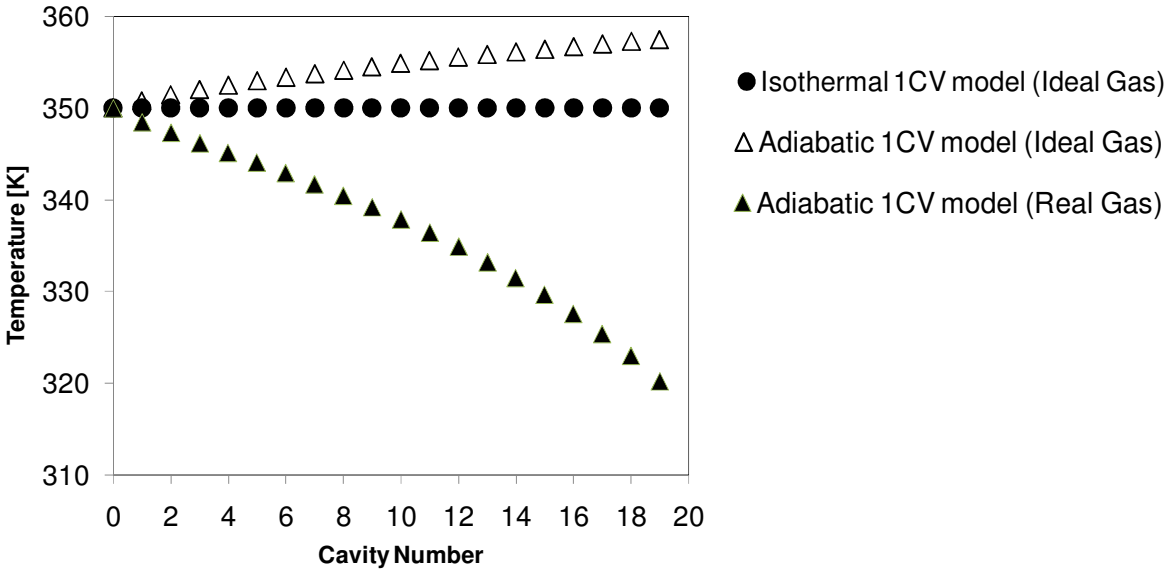

Figure 38 Temperature distribution along the seal length at rotor speed=10krpm for Carbon dioxide

The adiabatic flow model with ideal gas properties shows a rise in temperature along the seal length which can be attributed to the power transmitted from the rotor to the fluid by friction. The Adiabatic model with real gas properties however shows a significant drop in temperature. This can be explained by the fact that CO_2 has a positive Joule-Thompson coefficient (6 K/MPa) in the operating region. Thus, as the pressure drops there is a drop in temperature. For the present case, the drop in temperature due to Joule-Thompson effect is much higher than the rise in temperature due to power input.

Rotordynamic coefficients are evaluated for rotor speed of 3.6 krpm. Effective damping values are presented as they are critical to the stability of a rotordynamic system. Figure 39 shows that the adiabatic flow model with ideal gas properties is more conservative (yields lesser effective damping) at lower preswirl ratios. This is contrary to that obtained for Methane. The discrepancies can be explained in terms of the Z-factor.

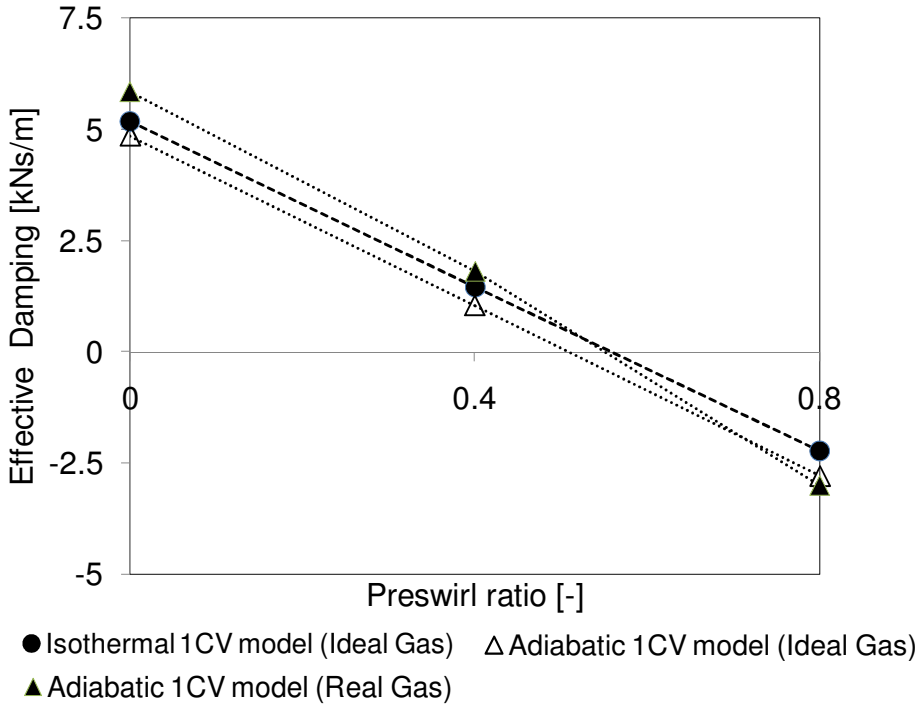

Figure 39 Effective damping versus preswirl ratio at rotor speed=3.6krpm for Carbon dioxide

Figure 40 shows higher magnitude of direct stiffness for the real gas model as compared to the other models. This can be attributed to the higher mass flow-rate predicted for the real gas model.

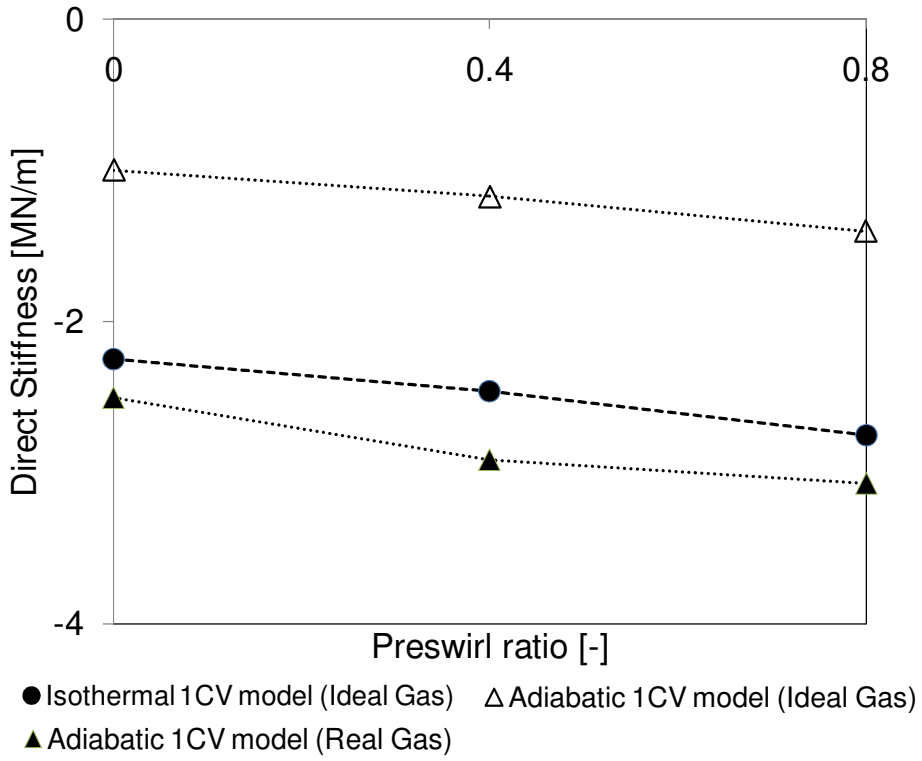

Figure 40 Direct stiffness versus preswirl ratio at rotor speed=3.6krpm for Carbon dioxide

Test cases with Methane and Carbon dioxide conclusively show the impact of real gas properties on predictions of flow and rotordynamic parameters in a labyrinth seal. Joule-Thompson effect which is characteristic of real gases has a significant impact on temperature distribution in a seal. However, temperature variations observed in the test cases do not significantly affect rotordynamic force predictions. Gas compressibility factor (Z) which is a measure of deviation of a gas from ideal behavior has a significant impact on leakage flow rate predictions. The Methane test case that indicates greater

than unity Z-factor yields lower calculated leakage rates using Adiabatic Real Gas Model. Similarly test case for Carbon dioxide yields significantly higher leakage rates using real gas model.

The Methane test case shows lower effective damping values at lower preswirl for real gas model whereas Carbon dioxide test case shows exactly opposite trend. The opposing trends can be accounted for by the opposing features of Z-factors for the two test cases. Direct stiffness coefficients also show a wide variation for the three models.

CHAPTER VII

SUMMARY AND RECOMMENDATIONS

Frequency dependency of rotordynamic coefficients is observed as rotor surface velocity approaches a significant fraction of Mach 1. A sample stability analysis indicates the invalidity of the use of conventional synchronous frequency independent rotordynamic coefficients as rotor surface velocity increases. Use of frequency dependent force coefficients is recommended for rotor surface velocities above ~0.3 times Mach 1.

A number of leakage models are analyzed, and their impact on predictions of rotordynamic coefficients is studied. Kinetic Energy (KE) carryover is found to be a dominant factor in determination of cross-forces of a straight-through labyrinth seal. A leakage model based on Hodkinson's [35] KE carryover and a constant flow-coefficient of 0.716 by Eser and Kazakia [36] yield reasonable leakage predictions for both high and low-pressure labyrinth seals. This leakage equation also improves the predictions in direct damping and cross-coupled stiffness as compared to the previous leakage models. However, the improvement is marginal, and the direct damping predictions are still substantially under-predicted when compared with test results by Picardo [17]. A logical alternative is to include as many physical processes which occur in an actual labyrinth seal in the model. The 2CV model by Scharrer [8] includes the vortex flow which is neglected in the present analysis. However, comparison of 2CV model predictions with experimental results by Picardo shows behavior similar to 1CV model.

Recent work by Saikishan [46] indicates that flow-coefficient of a straight through labyrinth seal is a function of axial Reynold's number. However, any improvement in cross-force predictions is not expected with Reynold's number dependency as indicated by closed-form solution by Millsaps & Martinez-Sanchez [20]. Comparison of CFD results by Moore [13] with experimental results suggests that regions upstream of inlet and downstream of exit also yield substantial contribution to

seal forces. Bulk flow codes neglect the perturbations in pressure and velocity in the upstream and downstream regions of the labyrinth seal, and may contribute to the discrepancy between measured and predicted values. Incorporating inlet and exit boundary conditions based on the inlet and exit flow conditions, in a bulk flow model may lead to improvement in predictions.

The 1CV model predicts that a converging-clearance labyrinth seal is more stable as compared to a diverging clearance labyrinth for excitation frequency greater than ~0.3 times rotor speeds for a Tooth-on-stator Labyrinth seal which qualitatively conforms to experimental results by Wright [16] and Kurohashi, et al. [5].

The inclusion of energy equation in the bulk flow model shows ambiguous predictions for rotordynamic coefficients. For low rotor speeds, the isothermal model and adiabatic model show marginal difference in predictions. However, as rotor speed increases, the adiabatic model performs better when compared with direct stiffness and cross-coupled damping. The isothermal model yields better predictions for direct damping and cross-coupled stiffness as compared to the adiabatic model. Influence of real gas properties on static and rotordynamic characteristics is studied for two test cases-Methane and Carbon dioxide. The results indicate a strong influence of Z-factor on leakage and rotordynamic characteristics of the seal.

Note that bulk flow codes offer a significant advantage over CFD based models in terms of computational time. The discrepancies between measurements and predictions clearly highlight the need for development of a bulk flow model with better correlations obtained via CFD calculations. Development of empirical relations based on parametric studies of CFD models and incorporating them in bulk flow models may further improve the predictions.

REFERENCES

[1] Alford, J.S., 1965, "Protecting Turbomachinery from Self-Excited Rotor Whirl," Journal of Engineering for Power, **87**, pp. 333-344.

[2] Kostyuk, A.G., 1972, "A Theoretical Analysis of the Aerodynamic Forces in the Labyrinth Glands of Turbomachines", Teploenergetica, **19**, pp.39-44.

[3] Spurk, J., Keiper, R., 1974, "Selbsterregte Schwingungen bei Turbomaschinen infolge der Labyrinthstrfmung," Archive of Applied Mechanics, **43**, pp. 127-135.

[4] Iwatsubo, T., Matooka, N., and Kawai, R., 1982, "Flow Induced Force and Flow Pattern of Labyrinth Seal," Proceedings of NASA CP 2250 workshop at Texas A&M University, Rotordynamic Instability Problems in High Performance Turbomachinery, pp.205-222.

[5] Kurohashi, M., Inoue,Y., Abe,T., and Fujikawa, T., 1980, "Spring and Damping Coefficients of the Labyrinth Seals," Paper No. C283/80, *Proceedings of the 2nd International Conference on Vibrations in Rotating Machinery* (Institution of Mechanical Engineers), held at Churchill College, Cambridge University, pp. 215-222.

[6] Childs, D., Scharrer, J., 1986, "An Iwatsubo-Based Solution for Labyrinth Seals: Comparison to Experimental Results", Journal of Engineering for Gas Turbines and Power, **108**, pp.325-331.

[7] Wyssman, H., Pham, T., and Jenny, R., 1984, "Prediction of Stiffness and Coefficients for Centrifugal Compressor Labyrinth Seals," Journal of Engineering for Gas Turbines and Power, **106**, pp.920-926.

[8] Scharrer, J., 1988, "Theory Versus Experiment for the Rotordynamic Coefficient of Labyrinth Gas Seals: Part I – A Two Control Volume Model," Journal of Vibration, Acoustics, Stress and Reliability in Design, **110**, pp.270-280.

[9] Tam, L. T., Przekwas, A. J., Muszynska, A., Hendricks, R. C., Braun, M. J., and Mullen, R. L., 1988, ''Numerical and Analytical Study of Fluid Dynamic Forces in Seals and Bearings,'' Journal of Vibrations and Acoustics, **110**, pp. 315–325.

[10] Nordmann, R., and Dietzen, F. J., 1988, ''Finite Difference Analysis of Rotordynamic Seal Coefficients for an Eccentric Shaft Position,'' NASA CP 3026.

[11] Rhode, D. L., Hensel, S. J., and Guidry, M. J., 1992, ''Labyrinth Seal Rotordynamic Forces Using a Three-Dimensional Navier-Stokes Code,'' Journal of Tribology, **114**, pp. 683–689.

[12] Athevale, M. M., Przekwas, A. J., Hendricks, R. C., and Liang, A., 1994,‘‘SCISEAL: A 3D CFD Code for Accurate Analysis of Fluid Flow and Forces in Seals,’’ *Proceedings of the Advanced ETO Propulsion Conference*, NASA CP3282, NASA Marshall Space Flight Center, May, Huntsville, AL, pp. 337–345.

[13] Moore, J., 2003, “Three-Dimensional CFD Rotordynamic Analysis of Gas Labyrinth Seals”, Journal of Vibrations and Acoustics, **125**, pp.427-433.

[14] Pelletti, J., 1990, ‘‘A Comparison of Experimental Results and Theoretical redictions for the Rotordynamic Coefficients of Short (L/D=1/6) Labyrinth Seals,’’ M.S. thesis, Texas A&M University, College Station.

[15] Wachter, J. **,** and Benckert, H. ,1978, “ Querkrafte aus Spaltdichtungen-Eine mogliche Ursache fur die Laufunruhe von Turbomaschinen,” Atomkernenerqie Bd. 32,Lfg. 4, pp. 239-2460.

[16] Wright, D.V., 1977,“Air Model Tests of Labyrinth Seal Forces On a Whirling Rotor,” Turbomachinery Development in Steam and Gas Turbines, Presented at Winter Annual Meeting of ASME, Atlanta, Ga., pp. 61-73.

[17] Picardo, A., 2003, “High Pressure Testing of See-Through Labyrinth Seals”, M.S. thesis, Texas A&M University, College Station.

[18] Kleynhans, G., and Childs, D., 1997, “The Acoustic Influence of Cell Depth on the Rotordynamic Characteristics of Smooth-Rotor/Honeycomb-Stator Annular Gas Seals,” Journal of Engineering for Gas Turbines and Power, **119**, pp. 949-957.

[19] Kanemitsu, Y., Ohasawa, M., 1986, “Experimental Study on Flow-Induced Force of Labyrinth Seal”, Proceedings, Post IFToMM Conference on Flow Induced Force in Rotating Machinery, Kobe, Japan, pp.106-112.

[20] Millsaps, K., Martinez-Sanchez, M., 1994, “Dynamic forces from single gland labyrinth seals: Part I-Ideal and Viscous Decomposition”, Journal of Turbomachinery, **186**, pp.686-693.

[21] Wagner, R., Steff, K., Gausmann R., Schmidt, M., 2009, “Investigations of Dynamic Coefficients of Impeller Eye Labyrinth Seals” 38th Turbomachinery Symposium, Houston.

[22] Thieleke, G., Stetter, H., 1990, “Experimental Investigations of Exciting Forces caused by Flow in Labyrinth Seals”, TAMU Instability Workshop.

[23] Neumann, K., 1964, “Zur Frage der Verwendung von Durchblicktungen im Dampgturbinebau,” Maschinentechnik, **13**(4).

[24] Vermes, G., 1961, "A Fluid Mechanics Approach to the Labyrinth Seal Leakage Problem", Journal of Engineering for Power, pp. 161-169.

[25] Gamal, A., 2007, "Leakage and Rotordynamic effects of Pocket Damper Seals and See-Through Labyrinth Seals", Ph.D Dissertation, Texas A&M University, College Station.

[26] McGreehan, F., Ko, H., 1989, "Power Dissipation in Smooth and Honeycomb Labyrinth Seals", ASME paper No. 89-GT-220.

[27] Millwards, J., Edwards, M., 1996, "Windage Heating of Air Passing Through Labyrinth Seals", Journal of Turbomachinery, **118**, pp.414-419.

[28] Denecke, J., Dullenkopf, K., Wittig, S., Bauer, H., 2005,"Experimental Investigation of the total Temperature increase and Swirl Development in Rotating Labyrinth Seals", ASME paper GT-2005-68677.

[29] Martinez-Sanchez, M., Lee, O.W.K., Czajkowski, E., 1984, "The prediction of Force Coefficients for Labyrinth Seals", Proceedings of Nasa CP 2338 workshop held at Texas A&M University, Rotordynamic Instability Problems in High Performance Turbomachinery, pp. 235-256.

[30] Gurevich, M.I. 1966, "The Theory of Jets in an Ideal Fluid", Pergamon Press, Oxford, pp. 319–323.

[31] Childs, D., Chang-Ho Kim,1984, "Analysis and testing of Rotordynamic Coefficients of Turbulent Annular Seals with Different, Directionally Homogeneous Surface-Roughness Treatment for Rotor and Stator Elements", Proceedings of Nasa CP 2338 workshop held at Texas A&M University, Rotordynamic Instability Problems in High Performance Turbomachinery, pp. 313-340.

[32] Bolleter, U., Leibundgut, E., Stürchler, R., and McCloskey, T., 1989, "Hydraulic Interaction and Excitation Forces of High Head Pump Impellers," in: PumpingMachinery—1989, Proceedings of the Third Joint ASCE/ASME Mechanical Conference, La Jolla, CA, pp. 187-194.

[33] Martin, January 19, 1908 H. M., "Labyrinth Packings," Engineering, pp. 35-36.

[34] Egli, A., 1935, "The Leakage of Steam through Labyrinth Seals," Transactions of ASME, **57**, pp. 115-122.

[35] Hodkinson, B., 1939, "Estimation of the Leakage through a Labyrinth Gland," Proceedings of the Institution of Mechanical Engineers, **141**, pp.283–288.

[36] Esser, D. and Kazakia, J. Y., 1995, “Air Flow in Cavities of Labyrinth Seals,” International Journal of Engineering Science, **33**, pp.2309-2326.

[37] Gans, B., 1983, “Prediction of the aero-elastic force in a labyrinth type seal and its impact on Turbomachinery stability”, MS thesis, MIT.

[38] Vance, J. M., Zierer, J. J., and Conway, E. M., 1993, "Effect of Straight Through Labyrinth Seals on Rotordynamics," *Proceedings of the 14th Vibration and Noise Conference*, Albuquerque, NM, ASME DE, **60**, pp. 159–171.

[39] Brownell, J., Millward, J., Parker, R., 1988, “Non-Intrusive Investigations into Life-Size Labyrinth Seal Flow Fields”, ASME paper 88-GT-45.

[40] Wang, W.Z., Liu, Y.Z., Chen,H.P., and Jiang, P.N., 2007,“ Computation of rotordynamic coefficients associated with leakage steam flow through labyrinth seal”, Archive of Applied Mechanics, **77** (8), pp. 587-597.

[41] The International Association for the Properties of Water and Steam: Release on the IAPWS industrial formulation 1997 for the thermodynamic properties of water and steam, Erlangen, Germany September (1997).

[42] Huber, M. L., 2003, NIST Thermophysical Properties of Hydrocarbon Mixtures Database (SUPERTRAPP), Version 3.1, U. S. Department of Commerce, National Institute of Standards and Technology, Standard Reference Data Program, Gaithersburg, MD.

[43] White, F., 2003, “Fluid Mechanics”, McGraw Hill, 5th Edition.

[44] Scharrer, J., 1989, “Rotordynamic coefficient for stepped labyrinth gas seals”, Journal of Tribology, **111**, pp.101–107.

[45] Shin, Y-S., and Childs, D.W., 2008, “The Impact of Real Gas Properties on Predictions of Static and Rotordynamic Properties of the Annular Gas Seals for Injection Compressors”, Journal of Engineering for Gas Turbines and Power, **130**, pp.042504.1-042504.8.

[46] Saikishan, S., 2009, “Labyrinth Seal Leakage Equation”, MS thesis, Texas A&M University, College Station.

APPENDIX A

Definition of first order coefficients

Continuity equation

$G_{1i} = \frac{A_{0i}}{RT_{0i}}$	$G_{8i} = \frac{\partial \dot{m}_{i+1}}{\partial P_i} - \frac{\partial \dot{m}_i}{\partial P_i}$
$G_{2i} = \frac{A_{0i} V_{0i}}{RR_s T_{0i}}$	$G_{9i} = -\frac{\partial \dot{m}_i}{\partial P_{i-1}}$
$G_{3i} = \frac{P_{0i} A_{0i}}{RR_s T_{0i}}$	$G_{10i} = \frac{\partial \dot{m}_{i+1}}{\partial P_{i+1}}$
$G_{6i} = \frac{L_i P_{0i}}{RT_{0i}}$	$G_{13i} = \frac{\partial \dot{m}_{i+1}}{\partial H_i} - \frac{\partial \dot{m}_i}{\partial H_{i-1}}$
$G_{7i} = \frac{P_{0i} V_{0i} L_i}{RR_s T_{0i}}$	

Circumferential momentum equation

$X_{1i} = \frac{A_{0i} V_{0i}}{RT_{0i}}$	$X_{9i} = V_{0i} \frac{\partial \dot{m}_{i+1}}{\partial P_i} - V_{0i-1} \frac{\partial \dot{m}_i}{\partial P_i} + as_i L_i \frac{\partial \tau_{si}}{\partial P_i} - ar_i L_i \frac{\partial \tau_{ri}}{\partial P_i}$
$X_{2i} = \frac{A_{0i} V_{0i}^2}{RR_s T_{0i}} + \frac{A_{0i}}{R_s}$	$X_{10i} = -V_{0i} \frac{\partial \dot{m}_i}{\partial P_{i-1}}$
$X_{3i} = \frac{P_{0i} A_{0i}}{RT_{0i}}$	$X_{11i} = V_{0i} \frac{\partial \dot{m}_{i+1}}{\partial P_{i+1}}$
$X_{4i} = \frac{2P_{0i} V_{0i} A_{0i}}{RR_s T_{0i}}$	$X_{12i} = \dot{m}_0 + as_i L_i \frac{\partial \tau_{si}}{\partial V_i} - ar_i L_i \frac{\partial \tau_{ri}}{\partial V_i}$
$X_{7i} = \frac{P_{0i} V_{0i} L_i}{RT_{0i}}$	$X_{13i} = -\dot{m}_0$
$X_{8i} = \frac{P_{0i} V_{0i}^2 L_i}{RR_s T_{0i}}$	$X_{16i} = V_{0i} \frac{\partial \dot{m}_{i+1}}{\partial H_i} - V_{0i-1} \frac{\partial \dot{m}_i}{\partial H_{i-1}}$

APPENDIX B

$$A_{11} = \frac{\partial \dot{\tilde{m}}_{0i}}{\partial p_{0i-1}}$$

$$A_{12} = 0$$

$$A_{13} = -\frac{\partial \dot{\tilde{m}}_{0i}}{\partial \tilde{h}_{0i-1}}$$

$$A_{21} = -v_{0i-1}\frac{\partial \dot{\tilde{m}}_{0i}}{\partial p_{0i-1}}$$

$$A_{22} = -1$$

$$A_{23} = -v_{0i-1}\frac{\partial \dot{\tilde{m}}_{0i}}{\partial \tilde{h}_{0i-1}}$$

$$A_{31} = -\left(\tilde{h}_e\tilde{h}_{0i-1} + \frac{v_{0i-1}^2}{2}\right)\frac{\partial \dot{\tilde{m}}_{0i}}{\partial p_{0i-1}}$$

$$A_{32} = -v_{0i-1}$$

$$A_{33} = -\tilde{h}_e - \left(\tilde{h}_e\tilde{h}_{0i-1} + \frac{v_{0i-1}^2}{2}\right)\frac{\partial \dot{\tilde{m}}_{0i}}{\partial \tilde{h}_{0i-1}}$$

$$B_{11} = \sigma_{0i}\frac{\partial \tilde{\rho}_{0i}}{\partial p_{0i}}\left(f - v_{0i}\right)\boldsymbol{j} + \frac{\partial \dot{\tilde{m}}_{0i+1}}{\partial p_{0i}} - \frac{\partial \dot{\tilde{m}}_{0i}}{\partial p_{0i}}$$

$$B_{12} = -\boldsymbol{j}\sigma_{0i}\tilde{\rho}_{0i}$$

$$B_{13} = \sigma_{0i}\frac{\partial \tilde{\rho}_{0i}}{\partial \tilde{h}_{0i}}\left(f - v_{0i}\right)\boldsymbol{j} + \frac{\partial \dot{\tilde{m}}_{0i+1}}{\partial \tilde{h}_{0i}}$$

$$B_{21} = \sigma_{0i}\left(v_{0i}\frac{\partial \tilde{\rho}_{0i}}{\partial p_{0i}}\left(f - v_{0i}\right) - P_e\right)\boldsymbol{j} + v_{0i}\frac{\partial \dot{\tilde{m}}_{0i+1}}{\partial p_{0i}} - v_{0i-1}\frac{\partial \dot{\tilde{m}}_{0i}}{\partial p_{0i}} + \sigma_{0i}\left(\lambda_s\frac{\partial \tilde{\tau}_{0si}}{\partial p_{0i}} - \lambda_r\frac{\partial \tilde{\tau}_{0ri}}{\partial p_{0i}}\right)$$

$$B_{22} = \sigma_{0i}\left(\tilde{\rho}_{0i}\left(f - 2v_{0i}\right)\right)\boldsymbol{j} + \sigma_{0i}\left(\lambda_s\frac{\partial \tilde{\tau}_{0si}}{\partial v_{0i}} - \lambda_r\frac{\partial \tilde{\tau}_{0ri}}{\partial v_{0i}}\right) + 1$$

$$B_{23} = \sigma_{0i}\left(v_{0i}\frac{\partial \tilde{\rho}_{0i}}{\partial \tilde{h}_{0i}}\left(f - v_{0i}\right)\right)\boldsymbol{j} + v_{0i}\frac{\partial \dot{\tilde{m}}_{0i+1}}{\partial \tilde{h}_{0i}} + \sigma_{0i}\left(\lambda_s\frac{\partial \tilde{\tau}_{0si}}{\partial \tilde{h}_{0i}} - \lambda_r\frac{\partial \tilde{\tau}_{0ri}}{\partial \tilde{h}_{0i}}\right)$$

$$B_{31}=\sigma_{0i}\left(\tilde{\rho}_{0i}\tilde{u}_e\frac{\partial\tilde{u}_{0i}}{\partial p_{0i}}f+\tilde{u}_{0i}\tilde{u}_e\frac{\partial\tilde{\rho}_{0i}}{\partial p_{0i}}f+\frac{v_{0i}^2}{2}\frac{\partial\tilde{\rho}_{0i}}{\partial p_{0i}}f-v_{0i}\tilde{h}_{0i}\tilde{h}_e\frac{\partial\tilde{\rho}_{0i}}{\partial p_{0i}}-\frac{v_{0i}^3}{2}\frac{\partial\tilde{\rho}_{0i}}{\partial p_{0i}}\right)\boldsymbol{j}$$
$$+\left(\tilde{h}_e\tilde{h}_{0i}+\frac{v_{0i}^2}{2}\right)\frac{\partial\dot{\tilde{m}}_{0i+1}}{\partial p_{0i}}-\left(\tilde{h}_e\tilde{h}_{0i-1}+\frac{v_{0i-1}^2}{2}\right)\frac{\partial\dot{\tilde{m}}_{0i}}{\partial p_{0i}}-\sigma_{0i}\lambda_r\frac{\partial\tilde{\tau}_{0ri}}{\partial p_{0i}}$$

$$B_{32}=\sigma_{0i}\left(v_{0i}\tilde{\rho}_{0i}f-\tilde{\rho}_{0i}\tilde{h}_{0i}\tilde{h}_e-\frac{3}{2}\tilde{\rho}_{0i}v_{0i}^2\right)\boldsymbol{j}+v_{0i}-\sigma_{0i}\lambda_r\frac{\partial\tilde{\tau}_{0ri}}{\partial v_{0i}}$$

$$B_{33}=\sigma_{0i}\left(\tilde{\rho}_{0i}\tilde{u}_e\frac{\partial\tilde{u}_{0i}}{\partial\tilde{h}_{0i}}f+\tilde{u}_{0i}\tilde{u}_e\frac{\partial\tilde{\rho}_{0i}}{\partial\tilde{h}_{0i}}f+\frac{v_{0i}^2}{2}\frac{\partial\tilde{\rho}_{0i}}{\partial\tilde{h}_{0i}}f-\tilde{\rho}_{0i}v_{0i}\tilde{h}_e-v_{0i}\tilde{h}_{0i}\tilde{h}_e\frac{\partial\tilde{\rho}_{0i}}{\partial\tilde{h}_{0i}}-\frac{v_{0i}^3}{2}\frac{\partial\tilde{\rho}_{0i}}{\partial\tilde{h}_{0i}}\right)\boldsymbol{j}$$
$$+\tilde{h}_e+\left(\tilde{h}_e\tilde{h}_{0i}+\frac{v_{0i}^2}{2}\right)\frac{\partial\dot{\tilde{m}}_{0i+1}}{\partial\tilde{h}_{0i}}-\sigma_{0i}\lambda_r\frac{\partial\tilde{\tau}_{0ri}}{\partial\tilde{h}_{0i}}$$

$$C_{11}=\frac{\partial\tilde{m}_{0i+1}}{\partial p_{0i+1}}$$
$$C_{12}=0$$
$$C_{13}=0$$
$$C_{21}=v_{0i}\frac{\partial\tilde{m}_{0i+1}}{\partial p_{0i+1}}$$
$$C_{22}=0$$
$$C_{23}=0$$
$$C_{31}=\left(\tilde{h}_e\tilde{h}_{0i}+\frac{v_{0i}^2}{2}\right)\frac{\partial\tilde{m}_{0i+1}}{\partial p_{0i+1}}$$
$$C_{32}=0$$
$$C_{33}=0$$

$$D_1=\sigma\tilde{\rho}_{0i}\beta_{0i}\left(f-v_{0i}\right)\boldsymbol{j}$$
$$D_2=\sigma\tilde{\rho}_{0i}v_{0i}\beta_{0i}\left(f-v_{0i}\right)\boldsymbol{j}+\sigma\left(\lambda_s\frac{\partial\tilde{\tau}_{0si}}{\partial\eta}-\lambda_r\frac{\partial\tilde{\tau}_{0ri}}{\partial\eta}\right)$$
$$D_3=\sigma\left(\tilde{u}_{0i}\tilde{u}_e\tilde{\rho}_{0i}\beta_{0i}f+\frac{1}{2}v_{0i}^2\tilde{\rho}_{0i}\beta_{0i}f-\tilde{\rho}_{0i}v_{0i}\tilde{h}_{0i}\tilde{h}_e\beta_{0i}-\frac{1}{2}\tilde{\rho}_{0i}v_{0i}^3\beta_{0i}\right)\boldsymbol{j}-\sigma\lambda_r\frac{\partial\tilde{\tau}_{0ri}}{\partial\eta}$$

The given set of equations is for a single cavity. The cavity equations are assembled to form a 6NC × 6NC matrix equation (NC = number of seal cavities). Pressure, velocity and enthalpy perturbations are assumed to be zero at the seal entry and exit.

The solution is of the form:

$$p_{1ic} = \frac{r_0}{\varepsilon} p'_{1ic}$$

$$p_{1is} = \frac{r_0}{\varepsilon} p'_{1is}$$

Radial and circumferential dynamic forces are evaluated from the pressure perturbations.

$$F_r(\Omega) = -R_s \pi L_i \varepsilon \sum_{i=1}^{NC} P_{1ic}$$

$$= -R_s \pi L_i P_R r_0 \sum_{i=1}^{NC} p'_{1ic}$$

$$= -\frac{R_s \pi L_i P_R R_0}{C_{r1}} \sum_{i=1}^{NC} p'_{1ic}$$

Similarly,

$$F_\theta(\Omega) = -\frac{R_s \pi L_i P_R R_0}{C_{r1}} \sum_{i=1}^{NC} p'_{1is}$$

The radial and circumferential dynamic stiffness coefficients are evaluated from these forces:

$$f_r(\Omega) = \frac{F_r(\Omega)}{R_0}$$

$$f_\theta(\Omega) = \frac{F_\theta(\Omega)}{R_0}$$

VITA

Manish Rambhau Thorat received his Bachelor of Engineering degree in mechanical engineering from Veermata Jijabai Technological Institute, Mumbai University, India in May 2007. He entered the mechanical engineering program at Texas A&M University in the Fall 2007 and received his Master of Science degree in May 2010. His research interests include vibrations and rotordynamics.

Turbomachinery Laboratory
c/o Dr. Dara Childs
Texas A&M University
3254 TAMU
College Station, Texas 77843-3254